Shallow-water equations and box model simulations of turbidity currents from a moving source

François Blanchette [*]

Department of Applied Mathematics, University of California Merced,
5200 N. Lake Road, Merced, California 95343, USA

We present numerical simulations of turbidity currents generated by a moving source that model particle clouds released by underwater vehicles such as those used in deep-sea dredging and mining. We use two approaches to model the flow and resulting deposits. First, we adapt the shallow-water equations to include a moving source of both momentum and particles. Second, we modify the classical box model to include a moving source. We validate our simulations before studying the impact of the most important governing dimensionless parameters: a vehicle Froude number Fr based on the depth of sediments being resuspended and the dimensionless settling speed of those sediments, u_s. We find that Fr is most determinant in the current and deposit shape, with Fr > 2 resulting in elongated shapes and Fr < 2 resulting in rounder ones, and that u_s determines the rate at which deposits grow. Another parameter, the vehicle's drag coefficient, was found not to have much effect beyond the immediate vicinity of the vehicle. Overall, both models found similar trends. The box model, much less computationally expensive, was less accurate when spatial nonuniformities developed, as happens at long times, but captured the early spreading rate well. The shallow-water equations handled nonuniformities correctly but tended to over-predict the spreading rate. We used the insight gained from those simulations to obtain criteria for the maximum extent of deposits left but such currents in both the low and high Froude number regimes.

I. INTRODUCTION

Deep-sea mining is an emerging field with both tremendous potential for the rare metal industry and considerable environmental risks. While industrial-scale deep-sea mining remains in the planning and exploratory stages, many operations are expected to begin in the next decade in the extensive international waters where polymetallic nodules can be found [1,2]. The environment where such operations would take place is difficult to study and remains only partially understood, although ongoing research, notably into the microbial ecology of polymetallic nodule fields, is helping further characterize it [3]. Even as our knowledge of these ecosystems remains partial, upcoming mining operations are being developed, threatening significant biodiversity loss [4]. Other than the immediate destruction where mining itself takes place, one of the most impactful aspect of deep-sea mining is the large sediment plume generated by the extraction process [5–7], which will likely affect a much broader area. We focus here on the spreading of such plumes in a quiescent environment.

The processes of collecting polymetallic nodules currently envisioned all involve a vehicle moving along the sea-floor. Such vehicles will disturb deposited sediments and are expected to

---
[*]fblanchette@ucmerced.edu

generate plumes of particulates in a manner similar to what may be seen when a land vehicle moves in a dry field. Because the ambient water near the sea-floor is nearly quiescent, the particulates themselves are likely to be dynamically significant in the spread of the resulting particle clouds. Recently, studies of the impacts of deep-sea mining on very large scales have been undertaken [5,6]. However, these studies do not take into consideration the local spread of these particle clouds, also known as turbidity currents or particle-laden currents, in the vicinity of the mining itself. In fact, few studies have considered such currents when generated by a moving source in any context, with the notable exception of the recently published direct numerical simulations of gravity currents released from a moving source [8]. These simulations identified two distinct regimes depending on the ratio of current spreading speed to vehicle speed. They also favorably compared their results to laboratory experiments, and in some cases to a much simpler box model (BM) which was found to adequately recover the spreading rate of the current in some cases. However, this study did not include suspended particles, which will be the main focus of the present work.

To allow for an efficient study of the impacts of deep-sea mining, we have developed simulations of gravity currents from moving sources that are averaged over the depth of the current. These are governed by the shallow-water equations (SWEs), which have been successfully used to describe ocean waves, including tsunamis [9], and gravity currents in a variety of contexts (see, for example, Refs. [10,11] and more recently Ref. [12]). However, they have never been applied to gravity currents spreading in two dimensions from a moving source. This approach involves one fewer dimension than direct simulations [8], making them much faster and allowing for the consideration of several types of particles, background flows as well as the optimization of a vehicular path to minimize environmental impacts. Smoothed particle hydrodynamics have been used to study deep-sea turbidites, including polydispersity and ocean current effects for stationary [13] and moving sources [14], though those studies include all effects simultaneously, making a direct comparison with our approach difficult. Despite the dimensionality reduction, such simulations, both shallow-water and smoothed particle hydrodynamics, still involve relatively large two-dimensional grids and therefore remain computationally demanding.

To obtain an even faster and more flexible model, we also incorporated a moving source into a box model [11], where quantities are averaged over the entire current. This approach has been used for several types of gravity currents [15–18]. In this method, we track averaged or total quantities. As a result, the system is described through ordinary differential equations only, and thus can be solved very quickly. However, some accuracy is lost. To better evaluate the advantages and disadvantages of each method and to quantify the degree of accuracy of the results obtained, we present a comparison of the results obtained by each method.

The remainder of this paper is organized as follows. We first present the governing equations in their most detailed form in Sec. II, before deriving the vertically averaged shallow-water equations in Sec. III and the box model in Sec. IV. We then describe the numerical methods used to solve each system in Sec. V before performing a validation, especially for the shallow-water equation, in Sec. VI. We present and compare results obtained by each model in Sec. VII and then conclude by discussing the applicability of both approaches in Sec. VIII.

II. GOVERNING EQUATIONS

We aim to capture the dynamics of a dilute particle-laden gravity current that is formed at the bottom of the ocean by the displacement of a dredging vehicle. The fluid motion is thus described by the incompressible Navier-Stokes equations where the suspension density, ρ, is variable [19]. The volume fraction of suspended particles, C, satisfies the advection-diffusion equation in which the particle velocity is given by $\boldsymbol{U_p} = \boldsymbol{U} - U_s\hat{\boldsymbol{k}}$, where $\boldsymbol{U}$ is the fluid velocity and U_s the particle settling speed [20]. This formulation is valid for small particle Stokes numbers, as is appropriate for
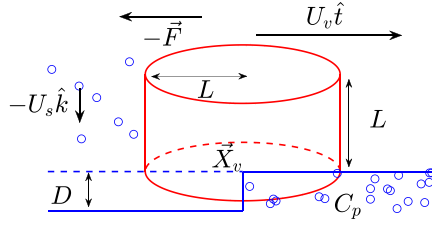
FIG. 1. Schematics of the parameters of the moving vehicle releasing particles into suspension.

fine sediments found on the ocean floor [21]. We thus consider the equations

$$\nabla \cdot \boldsymbol{U} = 0, \tag{1}$$

$$\rho\left(\frac{\partial \boldsymbol{U}}{\partial T} + (\boldsymbol{U} \cdot \nabla)\boldsymbol{U}\right) = -\nabla P + \mu\nabla^2\boldsymbol{U} - \rho g\,\hat{\boldsymbol{k}} + \boldsymbol{S_m}, \tag{2}$$

$$\frac{\partial C}{\partial T} + (\boldsymbol{U} - U_s\hat{\boldsymbol{k}}) \cdot \nabla C = \kappa\nabla^2 C + S_C, \tag{3}$$

where P is the fluid pressure, g is the gravitational acceleration, $\hat{\boldsymbol{k}}$ is an upward vertical unit vector, and κ the particle diffusion constant. We also introduced source terms: $\boldsymbol{S_m}$ is a momentum source with units of force per volume, and S_C is a particle source term with units of concentration per time. We use capital letters for dimensional quantities, and later will use lower case letters for dimensionless quantities.

To simplify the equations, we first consider the Boussinesq approximation, which assumes that the fluid density is constant, here taken to be the fluid density in the absence of particles ρ_0, except in the buoyancy term where density variations are multiplied by the gravitational acceleration. This approximation is valid when the density difference is less than 5% [22], which we expect to be the case in dilute currents. We also introduce a dynamic pressure, $P_d = P + \rho_0 gZ$, where Z is the vertical coordinate taken to increase from the ocean floor toward the surface. We further consider that the suspension density is linearly related to the particle volume fraction through

$$\rho = \rho_0\left(1 + \frac{\rho_s - \rho_0}{\rho_0}\,C\right) = \rho_0(1 + \Delta\rho_s C),$$

where ρ_s is the sediment density and we introduced the dimensionless density difference $\Delta\rho_s = \frac{\rho_s - \rho_0}{\rho_0}$. Finally, we introduce the dynamic viscosity, defined by $\mu = \nu\rho_0$. Equation (2) becomes, after dividing the momentum equation by ρ_0,

$$\frac{\partial \boldsymbol{U}}{\partial T} + (\boldsymbol{U} \cdot \nabla)\boldsymbol{U} = -\frac{\nabla P_d}{\rho_0} + \nu\nabla^2\boldsymbol{U} - \Delta\rho_s g\,C\,\hat{\boldsymbol{k}} + \frac{\boldsymbol{S_m}}{\rho_0}. \tag{4}$$

We consider source terms $\boldsymbol{S_m}$ and S_C that are centered on the vehicle's position, $\boldsymbol{X_v}(T)$, see Fig. 1. We assume that both the momentum and particle source term have the same horizontal distribution, $\Delta_2(\boldsymbol{X} - \boldsymbol{X_v})$, which has compact support on the scale of the vehicle size L and is such that $\int_{\mathbb{R}^2} \Delta_2(\boldsymbol{X})d\boldsymbol{X} = 1$. The vertical distribution relative to the ocean floor, where $Z = 0$, may be different for the momentum and concentration and we therefore denote them respectively as $\Delta_{1,m}(0)$ and $\Delta_{1,C}(0)$. We consider that the vehicle is subject to a hydrodynamic resistive force, or hydrodynamic drag, of $-\boldsymbol{F}$ and therefore exerts an equal and opposite force $\boldsymbol{F}$ on the fluid. The local force per volume, or momentum source, of the vehicle is thus $\boldsymbol{S_m} = \Delta_2(\boldsymbol{X} - \boldsymbol{X_v})\Delta_{1,m}(0)\boldsymbol{F}$. Focusing on the regime where the flow around the vehicle is turbulent, we approximate the resistive force using a high Reynolds number drag coefficient C_D as $\boldsymbol{F} = \hat{\boldsymbol{t}}C_D\rho_0 L^2 U_v^2$, where U_v is the vehicle speed and $\hat{\boldsymbol{t}}$ is a unit vector tangent to the vehicle's trajectory, as shown in Fig. 1. We

use a drag coefficient valid for spheres at large Reynolds numbers, which has been found to also be approximately applicable to trucks [23] of $C_D = \pi/10$, though we will also investigate the effects of varying C_D. We therefore use as a momentum source

$$\frac{\boldsymbol{S_m}}{\rho_0} = \Delta_2(\boldsymbol{X} - \boldsymbol{X_v}) \, \Delta_{1,m}(0) \, \hat{\boldsymbol{t}} \, C_D L^2 U_v^2. \tag{5}$$

For the particle source term, we consider that as the vehicle moves forward at speed U_v it scours deposited particles over a depth D from where particles become resuspended. Particles in the deposit have a packing fraction C_p so that, multiplying by the vehicle width L, the rate at which the mass of particulate gets released is

$$\frac{d\mathcal{M}}{dt} = C_e L \, D \, C_p \, \rho_s \, U_v,$$

where C_e stands for the fraction of removed sediments that becomes resuspended. Depending on the design of the vehicle, some sediment may be expelled smoothly enough so as to never become resuspended but for the purposes of this study we assume that all removed sediment becomes resuspended and set $C_e = 1$. To obtain the resuspended particle concentration rate, we divide the mass rate of change by ρ_s and multiply by the spatial distribution, finding

$$S_c = \Delta_2(\boldsymbol{X} - \boldsymbol{X_v}) \, \Delta_{1,C}(0) \, L \, D \, C_p \, U_v. \tag{6}$$

Nondimensionalization

To nondimensionalize the equations, we use the vehicle size, width, and height, L, as a typical length scale, and the vehicle's speed, U_v, as a velocity scale. We also use the pure fluid density, ρ_0, as a density scale. We define the maximum volume fraction of particles released as $C_m = \frac{D}{L}C_p$, which can be thought of as a rescaled ratio of the scoured depth, D, to the size of the vehicle L. We use C_m to rescale the particle volume fraction C. We write our nondimensional quantities in lower case as

$$t = \frac{U_v T}{L}, \quad \boldsymbol{x} = \frac{\boldsymbol{X}}{L}, \quad \boldsymbol{u} = \frac{\boldsymbol{U}}{U_v}, \quad p_d = \frac{P_d}{\rho_0 U_v^2}, \quad c = \frac{C}{C_m},$$

where we included the time (dimensional: T, dimensionless: t) and position vector (dimensional: $\boldsymbol{X}$, dimensionless: $\boldsymbol{x}$). In nondimensional form, our governing equations are

$$\nabla \cdot \boldsymbol{u} = 0, \tag{7}$$

$$\frac{\partial \boldsymbol{u}}{\partial t} + (\boldsymbol{u} \cdot \nabla)\boldsymbol{u} = -\nabla p_d + \frac{1}{\mathrm{Re}_v}\nabla^2 \boldsymbol{u} - \frac{c}{\mathrm{Fr}^2}\hat{\boldsymbol{k}} + s_m, \tag{8}$$

$$\frac{\partial c}{\partial t} + (\boldsymbol{u} - u_s\hat{\boldsymbol{k}}) \cdot \nabla c = \frac{1}{\mathrm{Pe}_v}\nabla^2 c + s_c, \tag{9}$$

with nondimensional numbers

$$\mathrm{Re}_v = \frac{U_v L}{\nu}, \quad \mathrm{Pe}_v = \frac{U_v L}{\kappa}, \quad u_s = \frac{U_s}{U_v}, \quad \text{and} \quad \mathrm{Fr} = \frac{U_v}{\sqrt{\Delta\rho_s C_m g L}} = \frac{U_v}{\sqrt{\Delta\rho_s C_p g D}},$$

which are, respectively, the vehicle Reynolds and Péclet numbers, dimensionless settling speed, and vehicle Froude number. The nondimensional sources are

$$\boldsymbol{s_m} = \frac{\boldsymbol{S_m} L}{\rho_0 U_v^2} = \hat{\boldsymbol{t}} \, C_D \, \delta_2(\boldsymbol{x} - \boldsymbol{x_v}) \, \delta_{1,m}(0) \quad \text{and} \quad s_c = \frac{S_C L}{C_m U_v} = \delta_2(\boldsymbol{x} - \boldsymbol{x_v})\delta_{1,C}(0),$$

where δ_2, $\delta_{1,m}$, and $\delta_{1,C}$ are dimensionless distribution functions.

It is possible to solve these equations, or very similar equations, directly. This has been done without source terms (e.g., Ref. [20]) and more recently with some source terms as well [8].

However, doing so remains very expensive computationally and therefore we proceed to develop a simplified model.

III. SHALLOW-WATER EQUATIONS

To obtain a system that can be solved at a smaller computational expense, we first associate a (nondimensional) height, h, to the gravity current. Such a height is typically defined as the region where the particle concentration exceeds a threshold value, such as $c > 0.01$. We then proceed to integrate the inviscid Navier-Stokes equations over the height of the current, to obtain the shallow-water equations. We ignore the fluid motion above and outside the current, as we consider that the currents of interest in deep-sea mining occur in a very deep ambient. The resulting single-layer shallow-water equations have been derived in details, for example, in Ref. [11], and we follow the same derivation.

Specifically, we define the average velocity and concentration as

$$\bar{\boldsymbol{u}} = \frac{1}{h} \int_0^h \boldsymbol{u} \, dz \quad \text{and} \quad \bar{c} = \frac{1}{h} \int_0^h c \, dz.$$

The presence of the source term and of the particle's settling require more careful attention. The latter can be integrated as

$$\int_0^h u_s \hat{\boldsymbol{k}} \cdot \nabla c \, dz = \int_0^h u_s \frac{\partial c}{\partial z} \, dz = u_s [c(h) - c(0)] \approx -u_s \, \bar{c},$$

where we used the approximations that at the top of the current the particle concentration is close to zero while at the bottom of the current it is close to the average particle concentration with the current.

To integrate the source terms, we need to specify the vertical distributions of momentum and of particles. We assume that the momentum is uniformly distributed over a (nondimensional) height of one, irrespective of the presence or absence of particles, so

$$\delta_{1,m}(0) = \begin{cases} 1 & \text{if } 0 \leqslant z \leqslant 1, \\ 0 & \text{otherwise.} \end{cases}$$

We then find upon integration that

$$\int_0^h \delta_{1,m}(0) \, dz = \min(h, 1).$$

In practice, we find that $h < 1$, so that this term is effectively just h.

For the concentration, the vertical distribution of particles always occurs over the height of the current, h, so that

$$\delta_{1,C}(0) = \begin{cases} \frac{1}{h} & \text{if } 0 \leqslant 1 \leqslant h, \\ 0 & \text{otherwise.} \end{cases}$$

We then find upon integration that

$$\int_0^h \delta_{1,C}(0) \, dz = 1.$$

In addition to the momentum and concentration equations, we consider the integration of the continuity equation. This yields an equation describing the time evolution of the current height itself. However, this height is now also subject to a source term. We model the release of particles as generating a source for the current height given by the vehicle speed, multiplied by the frontal area

of the vehicle and by the horizontal distribution function. In dimensionless terms, we thus have

$$\frac{\partial h}{\partial t} + \boldsymbol{\nabla} \cdot (h\bar{\boldsymbol{u}}) = \delta_2(\boldsymbol{x} - \boldsymbol{x}_v). \tag{10}$$

Usually, the shallow-water equations are derived assuming an inviscid flow (and no particle diffusion). However, it is convenient for numerical reasons to retain a diffusive term in those equations. Formally, we would like to consider

$$\nu_m = \frac{1}{\mathrm{Re}_n} \int_0^h \nabla^2 \boldsymbol{u} \, dz \approx \frac{1}{\mathrm{Re}_n} \left(\frac{\partial^2 (h\bar{\boldsymbol{u}})}{\partial x^2} + \frac{\partial^2 (h\bar{\boldsymbol{u}})}{\partial y^2} + \frac{\partial \bar{\boldsymbol{u}}}{\partial z} \Big|_{z=0}^{z=h} \right).$$

As this is retained for numerical convenience, we have introduced a numerical Reynolds number, Re_n, which only serves to stabilize simulations and typically takes values $\mathcal{O}(100)$ [24]. We also do not model the last term on the right and neglect its contribution, as the boundary friction is usually negligible at high Reynolds number. We approximate the remaining terms as the (horizontal) Laplacian of the integrated velocity over the height of the current

$$\nu_m \approx \frac{1}{\mathrm{Re}_n} \left[\frac{\partial^2 (\bar{\boldsymbol{u}} h)}{\partial x^2} + \frac{\partial^2 (\bar{\boldsymbol{u}} h)}{\partial y^2} \right] = \frac{1}{\mathrm{Re}_n} \nabla_h^2 (\bar{\boldsymbol{u}} h),$$

which will help avoid numerical instabilities. Similarly, we include a diffusive term for the particle concentration,

$$D_m \approx \frac{1}{\mathrm{Pe}_n} \nabla_h^2 (\bar{c} h).$$

Finally, we assume that the current height itself is subject to diffusive effects due to turbulent motion. We thus also include a diffusive term, $\frac{1}{\mathrm{Re}_n} \nabla_h^2 h$, to regularize the current height. The effect of these diffusive terms is expected to be small but numerically stabilizing, and this expectation will be verified explicitly in the validation section. We therefore find

$$\frac{\partial h}{\partial t} + \boldsymbol{\nabla} \cdot (h\bar{\boldsymbol{u}}) = \frac{1}{\mathrm{Re}_n} \nabla_h^2 h + \delta_2(\boldsymbol{x} - \boldsymbol{x}_v),$$

$$\frac{\partial h\bar{\boldsymbol{u}}}{\partial t} + \boldsymbol{\nabla} \cdot (h\bar{\boldsymbol{u}}\bar{\boldsymbol{u}}) = \frac{1}{\mathrm{Re}_n} \nabla_h^2 (h\bar{\boldsymbol{u}}) - \frac{1}{2\mathrm{Fr}^2} \boldsymbol{\nabla}(\bar{c}h^2) + \delta_2(\boldsymbol{x} - \boldsymbol{x}_v) \, \hat{\boldsymbol{t}} \, C_D \min(h, 1),$$

$$\frac{\partial h\bar{c}}{\partial t} + \boldsymbol{\nabla} \cdot (h\bar{\boldsymbol{u}}\bar{c}) + u_s \bar{c} = \frac{1}{\mathrm{Pe}_n} \nabla_h^2 (h\bar{c}) + \delta_2(\boldsymbol{x} - \boldsymbol{x}_v).$$

To facilitate the numerical formulation of this system, we introduce variables that appear directly in the time derivatives. We thus rewrite our system in terms of the current height, h, integrated velocity $\boldsymbol{q} = h\bar{\boldsymbol{u}}$ and integrated concentration $\phi = h\bar{c}$. Our system of equations is therefore

$$\frac{\partial h}{\partial t} + \boldsymbol{\nabla} \cdot \boldsymbol{q} = \frac{1}{\mathrm{Re}_n} \nabla_h^2 h + \delta_2(\boldsymbol{x} - \boldsymbol{x}_v), \tag{11}$$

$$\frac{\partial \boldsymbol{q}}{\partial t} + \boldsymbol{\nabla} \cdot \left(\frac{\boldsymbol{q}\boldsymbol{q}}{h}\right) = \frac{1}{\mathrm{Re}_n} \nabla_h^2 \boldsymbol{q} - \frac{1}{2\mathrm{Fr}^2} \boldsymbol{\nabla}(h\phi) + \delta_2(\boldsymbol{x} - \boldsymbol{x}_v) \, \hat{\boldsymbol{t}} \, C_D \min(h, 1), \tag{12}$$

$$\frac{\partial \phi}{\partial t} + \boldsymbol{\nabla} \cdot \left(\phi \frac{\boldsymbol{q}}{h}\right) + u_s \frac{\phi}{h} = \frac{1}{\mathrm{Pe}_n} \nabla_h^2 \phi + \delta_2(\boldsymbol{x} - \boldsymbol{x}_v). \tag{13}$$

Should the vehicle come to a stop, all the sources associated with it would vanish, corresponding to setting to zero all the terms multiplying δ_2.

Finally, as a diagnostic tool, we will keep track of the height of deposited particles, b. Particles are eroded by the vehicle and deposited as they settle out of the current, resulting in

$$\frac{\partial b}{\partial t} = \frac{D}{L}[u_s \bar{c} - \delta_2(\boldsymbol{x} - \boldsymbol{x}_v)] = \frac{D}{L}\left[u_s \frac{\phi}{h} - \delta_2(\boldsymbol{x} - \boldsymbol{x}_v)\right].$$
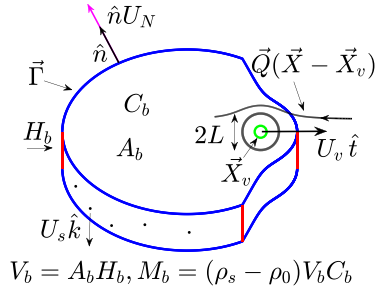
FIG. 2. Schematics of the box model used to approximate the gravity current spreading from a moving vehicle.

IV. BOX MODEL

While Eqs. (11)–(13) can be solved numerically, it remains relatively computationally expensive to do so. It may therefore be advantageous to simplify them even further to obtain a system of equations that can solved numerically very quickly. This can prove particularly useful when evaluating environmental consequences of dredging, which can involve a wide range of conditions. With such applications in mind, we introduce a corresponding box model, where the relevant quantities are averaged horizontally over the extent of the current. The model only tracks in time a couple of scalar quantities, the current volume and particle concentration, as well as the position of the current boundary boundary. The result is much simpler and easier to solve, but may suffer from a lack of detail and accuracy. In following sections, we compare results obtained by the box model and by the shallow-water equations simulations to determine when each model is most useful.

To obtain a (dimensional) box model, we begin by defining a boundary of the current, $\boldsymbol{\Gamma}$, within which we consider the particle concentration to be nonzero and outside of which we assume that no particles are in suspension, see Fig. 2. This boundary is assumed to be piecewise smooth and a simple closed curve. Its interior area, denoted by A_b, may be obtained directly from $\boldsymbol{\Gamma}$. We also define a current height, H_b, and a particle concentration C_b, which are assumed to be averaged horizontally over the entire current and are therefore functions of time only. The volume of the current is then $V_b = A_b H_b$ and the excess mass of the current, M_b, due to suspended particles is then expressed as

$$M_b = (\rho_s - \rho_0)V_b C_b. \tag{14}$$

The rate of change of the volume is found by integrating over the horizontal extent of the current the source term in Eq. (11) which gives, in dimensional form

$$\frac{dV_b}{dT} = U_v L^2. \tag{15}$$

The rate of change of the excess mass of suspended particle is the sum of the source of particles that is the vehicle, and the loss of particles through settling over the entire area of the current:

$$\frac{dM_b}{dT} = LDU_v\, C_p(\rho_s - \rho_0) - A_b U_s C_b(\rho_s - \rho_0). \tag{16}$$

Combining Eqs. (14), (15), and (16), we find an equation for the rate of change of the concentration:

$$\frac{dC_b}{dT} = \frac{LDC_pU_v - C_bL^2U_v - A_bU_sC_b}{V_b} = \frac{LDC_pU_v}{V_b}\left(1 - \frac{C_bL}{C_pD}\right) - \frac{U_sC_b}{H_b}. \tag{17}$$

Finally, we describe the motion of the boundary following box models presented, among others, by Hogg *et al.* [16]. In the absence of a vehicle, the so-called nose condition states that the spreading is driven by an imbalance in hydrostatic pressures so that $U_N = C_F\sqrt{H_bC_bg\Delta\rho_s}$, where U_N is the

nose velocity in a direction normal to the boundary, C_F current Froude number that is typically taken to be a constant between 1.19 [25] and $\sqrt{2}$ [26] depending on the depth of the surrounding fluid). In addition, we associate a flow to the moving vehicle, denoted as $U_v \boldsymbol{Q}(\boldsymbol{X} - \boldsymbol{X_v})$, where $\boldsymbol{X_v}$ is the position of the vehicle. This flow is assumed to take the form of an inviscid flow around a cylinder when at a distance greater than L from the vehicle, and otherwise to be a linear interpolation between the velocity of the vehicle at the location of the vehicle and the inviscid flow at a radius L away. The choice of an inviscid flow filed around a cylinder is appropriate ahead of the vehicle, where the flow is less affected by the specific design of the vehicle. Behind the vehicle, the flow is generally more complicated with a turbulent wake and streamline separation. However, in a box model, the boundary of the current is always ahead of the vehicle and is therefore unaffected by the wake. Specifically, we have the following spatial dependence of the flow, $\boldsymbol{Q}(\boldsymbol{X})$, for a vehicle located at the origin and moving in a direction $\hat{\boldsymbol{t}}$

$$\boldsymbol{Q}(X, Y) = \begin{cases} \frac{L^2}{R^4} \begin{pmatrix} \hat{\boldsymbol{t}} & \hat{\boldsymbol{k}} \times \hat{\boldsymbol{t}} \end{pmatrix}^{\mathrm{T}} \begin{pmatrix} X^2 - Y^2 \\ 2XY \end{pmatrix} & \text{if } R^2 \geqslant L^2, \\ \left(1 - \frac{R}{L}\right) \hat{\boldsymbol{t}} + \left(\frac{R}{L}\right) \boldsymbol{Q}(\frac{XL}{R}, \frac{YL}{R}) & \text{if } R^2 < L^2, \end{cases}$$

where we denote the distance to the vehicle as $R = \sqrt{X^2 + Y^2}$. Only the normal component of the flow will affect the normal displacement of the boundary, so in all we move the boundary according to

$$\frac{d\boldsymbol{\Gamma}}{dT} = \hat{\boldsymbol{n}}[C_F \sqrt{H_b C_b g \Delta \rho_s} + U_v \boldsymbol{Q}(\boldsymbol{X} - \boldsymbol{X_v}) \cdot \hat{\boldsymbol{n}}], \tag{18}$$

where $\hat{\boldsymbol{n}}$ is a unit outward normal to the curve $\boldsymbol{\Gamma}$.

In dimensionless form, using the same nondimensionalization as above, we therefore obtain the following system of differential equations:

$$\frac{dv_b}{dt} = 1, \tag{19}$$

$$\frac{dc_b}{dt} = \frac{1 - c_b}{v_b} - \frac{u_s a_b c_b}{v_b}, \tag{20}$$

$$\frac{d\boldsymbol{\gamma}}{dt} = \hat{\boldsymbol{n}} \left[\frac{C_F}{\mathrm{Fr}} \sqrt{\frac{v_b c_b}{a_b}} + \boldsymbol{q}(\boldsymbol{x} - \boldsymbol{x_v}) \cdot \hat{\boldsymbol{n}} \right], \tag{21}$$

where we have eliminated the current height h_b from the equations and the area, a_b can be obtained directly from the position of the boundary $\boldsymbol{\gamma}$. Also, should the vehicle come to a stop, all the sources associated with it would vanish, corresponding to setting to zero all the terms on the right-hand side of our system of equations except for the settling term (involving u_s) and the spreading term (involving Fr).

We can also recover an equation for the height of the deposited particles

$$\frac{\partial b_b}{\partial t} = \frac{D}{L} [\delta_b(x, y) u_s c_b - \delta_2(\boldsymbol{x} - \boldsymbol{x_v})], \tag{22}$$

where $\delta_b(x, y)$ is a function indicating if a point (x, y) is inside the current, where $\delta_b(x, y) = 1$, or outside the current, where $\delta_b(x, y) = 0$.

V. NUMERICAL IMPLEMENTATION

To capture the spread of a gravity current from a moving source, we implement a numerical solver for Eqs. (11)–(13). For the time integration, we use a Runge-Kutta method of order two. To discretize spatial derivatives, we need to be more careful, as the front of the current is, theoretically, a shock between positive values of the current height within the current and a zero value of the height outside the current. To handle this discontinuity accurately, we compute advective terms

using a third order upwinding WENO method [27]. This method greatly reduces oscillations near the front of the current, but numerical issues remain owing to the factor of $\frac{1}{h}$ that appears in Eqs. (12) and (13), or alternatively because the shallow-water equations are not properly defined when the current height is zero. While numerical methods that can handle wet/dry transitions have been developed [9,28], they are not directly applicable in the presence of a source that can smoothly increase the current height from zero to a finite nonzero value. We therefore use instead the Artificial Bed method [10,12], which assigns a small nonzero value, $h = h_m$, to the current height outside the current proper, called minimum current height. In the limit of $h_m \to 0$, we recover the formulation given above, but small nonzero values of h_m allow for stable simulations by avoiding numerical divisions by zero, or values extremely close to zero.

The other regularizing component of the simulations are the Laplacian terms, which are computed using centered finite differences. To reduce the number of parameters and avoid having different requirement on the time step for different diffusive terms, we make the common assumption that the numerical Reynolds and Péclet numbers are equal (e.g., Ref. [20]) so that $\mathrm{Re}_n = \mathrm{Pe}_n$.

In the simulations presented here, the grid used was uniform and fixed in space, though more efficient simulations could be performed by relaxing both of those conditions. To represent the spatial distribution of the source around the vehicle, we use an approximation of the delta function with radius one suggested by Peskin [29] which integrates to one and closely approximates other properties of the delta function

$$\delta_2(\boldsymbol{x}) = \delta_2(x, y) = \begin{cases} \frac{[1+\cos(\pi x)][1+\cos(\pi y)]}{4} & \text{if } \sqrt{x^2 + y^2} \leqslant 1, \\ 0 & \text{otherwise.} \end{cases}$$

To close the system, we must provide boundary conditions. Here, for simplicity, we use periodic conditions in both horizontal coordinates. As the current approaches the boundary, it will eventually be affected by the choice of boundary conditions, so we restrict our attention to times prior to when the current comes within one vehicle length from the boundary. Finally, to initiate the process, we use the least arbitrary initial conditions possible: we start from rest, with no suspended particles. The current is therefore only formed by particles suspended by the moving vehicle, and does not compete with a current spreading because of some initial suspension.

To solve the box model equations, Eqs. (19)–(21), we use a simple Runge-Kutta method of order two to march forward in time the concentration equation (and the volume equation, though that can also be solved exactly). To move the boundary, we first discretize its location by introducing markers that are no further apart that Δs_m. Each marker is also moved forward in time using a second order Runge-Kutta method. After markers have been moved, a periodic cubic spline interpolation based on arc length along the curve, s, is used to redistribute markers at every time step to keep them evenly spread. The area within the current is computed using the line integral

$$a_b = \int_{\boldsymbol{\gamma}} \frac{1}{2}\left(-\gamma_y \frac{d\gamma_x}{ds} + \gamma_x \frac{d\gamma_y}{ds}\right) ds,$$

where γ_x and γ_y are the x and y components of $\boldsymbol{\gamma}$, respectively, and $\frac{d\gamma_x}{ds}$ and $\frac{d\gamma_y}{ds}$ the components of their unit tangent vectors. This integral is evaluated numerically using a trapezoidal quadrature method, and the tangent vectors are obtained directly from the cubic spline interpolation.

The box model does not require any boundary condition as the current can spread indefinitely. However, an initial current must be specified to provide an initial boundary location. We thus initialize the current as a circle centered on the vehicle with a radius of R_0. We note that small values of the initial radius are sensitive to the form of the fluid velocity near the vehicle and require finer time and space resolutions.

The only modeling parameter in the box model is the constant C_F, which relates the front propagation speed to the square root of the current height, $\sqrt{v_b/a_b}$. For two-dimensional currents, this constant was theoretically found to be $C_F = \sqrt{2}/2$ is an idealized frictionless case in a tube [26], and was measured empirically to be somewhat larger in unidirectional spreading, with a theoretical
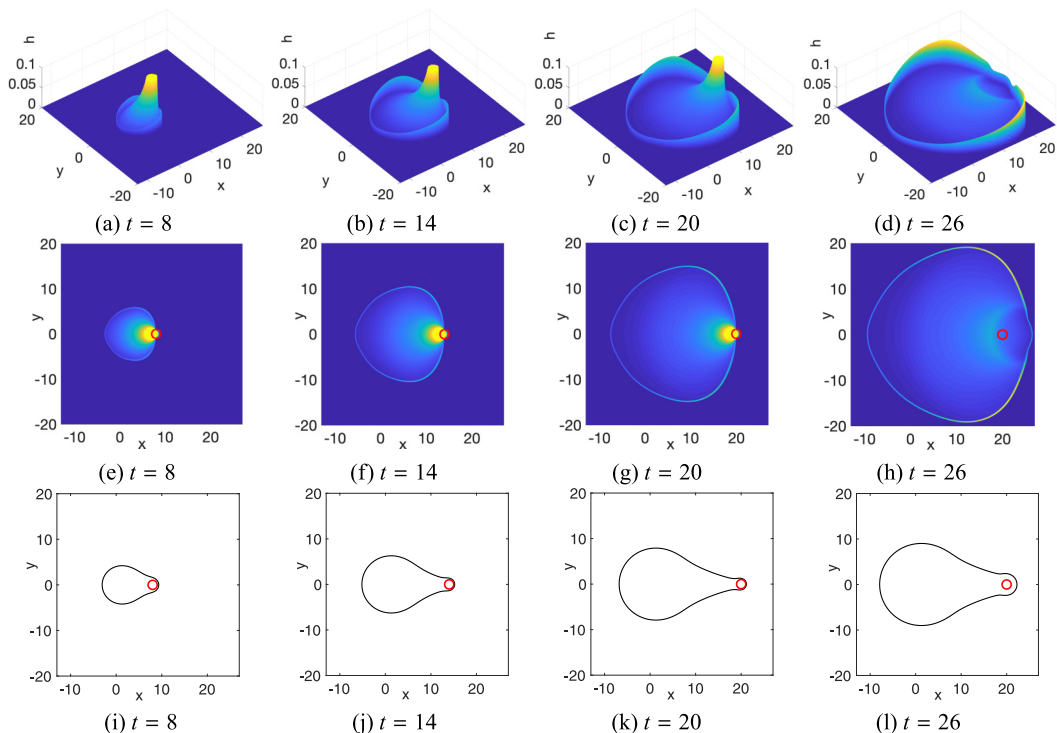
FIG. 3. [(a)–(h)] Simulated spreading of a deep-sea cloud generated by a dredging vehicle modeled by the shallow-water equations. [(i)–(l)] Same current simulated using a box model. The current height h is shown from the side [(a)–(d)] and from above [(e)–(h)]. In panels [(a)–(d)], the height was truncated to better show the current away from the vehicle, with the actual maximum height reaching $h = 0.88$. The vehicle, shown as a red circle in panels [(e)–(l)] starts at (0,0) and moves toward the positive x axis until $t = 20$, when it stops. Physical parameters are $\mathrm{Fr}^2 = 2$, $u_s = 0.01$, $C_D = \pi/10$ and for the box model $C_F = 1.2$. Numerical parameters for the shallow-water solver are $\Delta x = 0.025$, $\Delta t = 0.0025$ (so CFL $= 0.1$), $h_m = 0.001$, $\mathrm{Re}_n = 500$, and for the box model $\Delta t = 0.002$, $\Delta s_m = 0.025$, and $R_0 = 0.1$.

value of $\sqrt{2}$ in a deep ambient [30], and an empirically measured value of $C_F \approx 1.2$ [25]. We therefore set $C_F = 1.2$ in the remainder of this paper.

VI. VALIDATION

We begin by providing a sample of the computed current height over time as obtained by the shallow-equations solver, see Figs. 3(a)–3(h) and by the box model, Figs. 3(i)–3(l). Here the vehicle is moving toward the positive x axis until time $t = 20$, at which point it stops and the current continues to spread. The maximum current height, not shown to emphasize current features away from the vehicle, is approximately $h = 0.88$. There is qualitative agreement between the two approaches, and we will compare them more closely in the next section.

A. Box model solver validation

The box model contains relatively few numerical difficulties and parameters. In the present implementation, the only numerical parameters present in the box model solver are the time step, Δt, the maximum spacing between boundary markers, Δs_m, and the initial current radius, R_0. In certain nonconvex configurations, if the first two parameters are too large the interface crosses itself
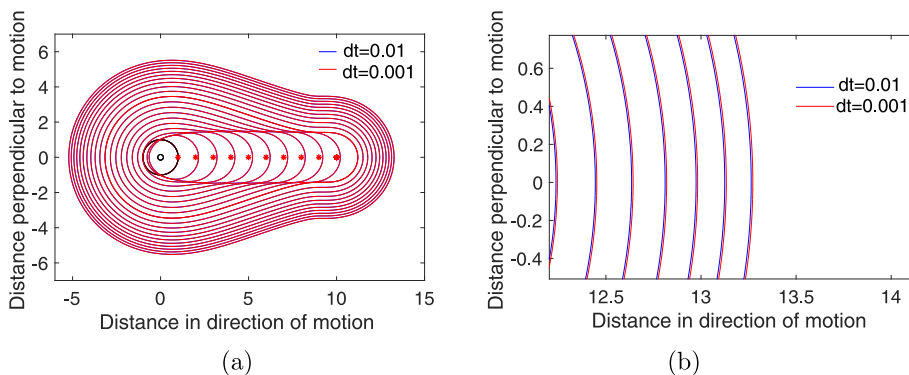
FIG. 4. (a) Sample calculation of the current height at various times for two choices of time step Δt. We indicate the position of the vehicle with a red star. Each curve is one time-unit apart and the black curve and circle are the initial current extent and vehicle position, respectively. (b) Closeup of the front of the current. The difference in distance traveled is less than 0.1%.

resulting in an ill-defined boundary and trapping a current-free bubble within the current. However, in the setups we considered and present here, this was not an issue. We set $\Delta s_m = 0.05$, and for validation simulated an identical system for $\Delta s = 0.025_m$, which showed no visible difference, with the maximum progression of the current being within 0.001% of each other. In those simulations, we set $\Delta t = 0.01$. Reducing the time step by a factor of 10, to $\Delta t = 0.001$, resulted in very minor differences in current progression, about 0.1%, as shown in Fig. 4.

The initial radius used had a direct impact on the distance spread, as larger R_0 naturally spread further, especially in the direction opposite the vehicle motion. The differences in spreading in three different directions (against vehicle motion, with vehicle motion, perpendicular to vehicle motion) are shown for three initial radii in Table I. The differences stayed about constant in time, and keeping in mind that the current will usually spread over distances of order 10 in this study, these differences are found to be quite small. Using values of R_0 smaller than 0.1 required finer time and space resolutions than desirable at later times, so we elected to use $R_0 = 0.1$ in the remainder of this study. We note that if the source position is kept fixed, our box model predicts a current spreading radially with radius $r = 0.95t^{3/4}/\mathrm{Fr}^{1/2}$, which is similar to but faster than that reported in the stationary box model results of Ref. [8] (which themselves agreed well with direct numerical simulations), where the multiplicative factor was 0.74, after conversion to our nondimensionalization. This difference is attributable to the choice of $C_F = 1.2$ which was made to capture current spreading unidirectionally rather than radially. We therefore expect our results to be more accurate when the motion of the source is faster than the current spread. In the regime studied here where settling is much slower than the source's speed, the integral of the particle concentration over the depth of a current is approximately H_bC_b in the box model formulation and C_pD in the shallow-water formulation. The

TABLE I. Differences in spreading distances as a function of R_0 toward the back, front, and side of the current, as defined relative to the direction of motion of the vehicle. Distances are measured at time $t = 4$.

R_0	Diff. back	Diff. front	Diff. side
0.05	N/A	N/A	N/A
0.1	0.1	0.001	0.01
0.2	0.35	0.002	0.06

TABLE II. Parameters used to perform numerical validations of the shallow-water equation solver.

Parameter	Value
Fr^2	2
u_s	0.01
C_D	0
Δx	0.05
Δt	0.005
$CFL = \Delta t / \Delta x$	0.1
h_m	0.001
Re_n	250
Domain size	20
Final time	13

Froude number therefore captures the ratio of the vehicle to current speed for both the SWE and BM models and our results will be most accurate when $Fr \gtrsim 1$.

B. Shallow-water solver validation

Solving the shallow-water equations is more challenging numerically and requires the introduction of additional numerical parameters. We require a spatial discretization size, Δx, a time step, Δt, minimum current height, h_m, and (inverse) numerical diffusion coefficient Re_n. We use a basic set of numerical and physical parameters, given in Table II, and then vary one numerical parameter at a time to determine its impact. Here, we set the drag coefficient, C_D, to zero to focus on the effects of the spreading current. The domain size and final time were kept constant throughout.

To evaluate the accuracy of the shallow-water solver, we consider a setup similar to that shown in Fig. 3, where a vehicle moves to the right and then stops at time $t = 10$. We will evaluate the accuracy of the dynamics of the current by looking at a cut of the current height h in the y direction at the location $x = 5$ (the vehicle traveled from $x = 0$ to $x = 10$). We show in the following figures only half of the domain, as the other half is the same by symmetry. In addition, we also consider the height of the deposited particles, as a measure of the long-term effects of the current. In fact, this deposit is arguably the most important feature of such currents as it is representative of the impact of the current on its overall environment. We show the deposit height normalized by D/L and do not show the deposit very close to the center line, since at that location it is dominated by the erosion due to the vehicle, with a normalized depth of $b \approx -1$.

We first show in Fig. 5 the effect of changing the CFL number, or ratio $\Delta t / \Delta x$ by changing Δt and keeping Δx fixed. In the regime considered, the effects of Δt are very small overall, and particularly small for the height of the deposit. Using too large a time step eventually results in instabilities, and those considerations are ultimately the most determinant in the choice of a CFL number as the accuracy is only weakly affected otherwise. Oscillations hinting at the onset of instability can be seen in the closeup for the largest CFL value shown (CFL = 0.4).

In Fig. 6, we consider the effects of varying the spatial resolution, Δx. As was the case when varying Δt, we find that the current and deposited particle profiles are nearly independent of the spatial resolution used in the range explored. Even zooming in on the most sensitive areas reveals only very minor differences between $\Delta x = 0.05$ and $\Delta x = 0.0125$. Here too, the biggest consideration in selecting a spatial resolution will be the stability of the simulations as other parameters, like the numerical Reynolds number and minimum current height, are changed.

The choice of the minimum current height h_m is seen in Fig. 7 to have a more significant influence on the current profile. As the current spreads away from the vehicle, it effectively plows into the region of minimum thickness, resulting in an accumulation at the edge of the current, the height and width of which depend on h_m. Varying from $h_m = 0.008$ to $h_m = 0.001$ shows that smaller values
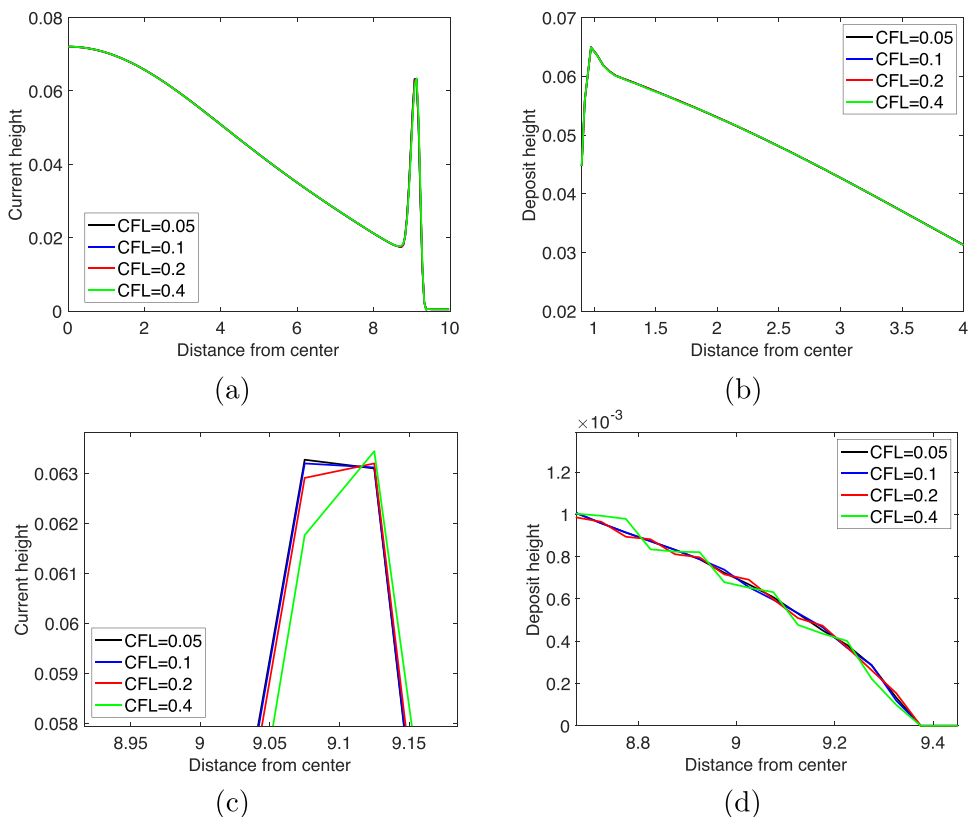
FIG. 5. (a) Current height and (b) resulting deposit height normalized by D/L for various CFL ratios obtained by varying the time step Δt. Other parameters are as shown in Table II and we show a cut from the center of the domain in a direction perpendicular to the vehicle motion. [(c), (d)] Closeups emphasizing the region where variations are most pronounced.

correspond to a faster spread and a smaller current head. Using a smaller h_m is more physically accurate, and the maximal height of the current should probably be lower than even that shown with the smallest h_m used. Unfortunately, using too small a value of h_m results in instabilities, unless a sufficiently small Δx and Δt are used, which becomes computationally very expensive. However, the most important long-term feature of the flow, the height of the deposited particles, show only a very weak dependence on h_m. The only effect is at the current's edge, where larger values of h_m that slow the spread of the current correspondingly show a deposit having reached a shorter distance away from the vehicle. However, at later times, the current would continue to spread and result in a deposit profile similar for all h_m, as is seen behind the very front of the current, say for $y < 6.5$ in Figs. 7(b) and 7(c).

Finally, the influence of the numerical choice of Re_n is shown in Fig. 8. Inversely to h_m for which smaller values are more relevant, larger values of Re_n corresponds to less numerical diffusion and are therefore preferable. However, smaller values of Re_n broaden the sharpest features of the current, such as the current head, and therefore hinder numerical instabilities. We see in Fig. 8 that as was the case for small h_m, using larger values of Re_n results in a faster spread, but avoiding numerical instabilities at higher Re_n requires finer spatial and temporal resolutions. Unlike small values of h_m, the more physical choice of a larger Re_n causes a higher maximum current height and a thinner current head. While this effect should plateau for high enough Re_n, with the resolution used such
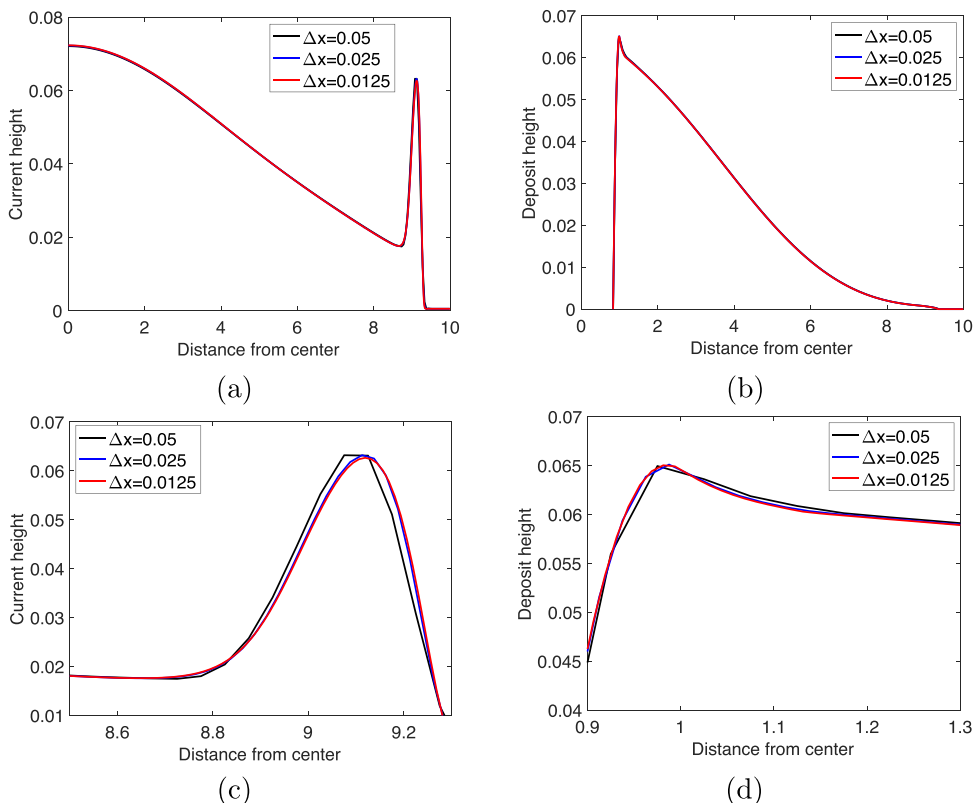
FIG. 6. (a) Current height and (b) resulting deposit height normalized by D/L for various values of Δx. Other parameters are as shown in Table II and we show a cut from the center of the domain in a direction perpendicular to the vehicle motion. [(c), (d)] Closeup emphasizing the region where variations are most pronounced.

a plateau was not reached. However, once again the particulate deposit height is only very weakly affected by the exact choice of Re_n. The only significant effect is at the front of the current, which is reached earlier at higher Re_n. So, particularly for $Re_n \geqslant 250$, the effect of Re_n on the deposit height is negligible.

We show in Fig. 9 the shape of the current, indicated by the level curve where $h = 2h_m$, for various numerical Reynolds numbers and minimum current height h_m. As noted before, the current spread faster, which is most visible at the top and bottom right portions of the current, for large numerical Reynolds numbers and small minimum current heights. The current shape is only weakly dependent on Re_n provided $Re_n \geqslant 250$. The dependence on h_m is more significant, but all the qualitative features of the current are unchanged for $h_m \leqslant 0.002$ and even the quantitative features such as the angle of the front with the horizontal are only weakly affected. We also note that this effect becomes even less pronounced when the vehicle's momentum is included $C_D > 0$, as it affects the current much more evenly for all values of h_m.

To validate our simulation results against known results, we computed the progression of a two-dimensional current in the absence of a source, as shown in Fig. 10. Using $h_m = 0.001$ and $Re_n = 500$, we recovered the slumping phase where the spreading velocity is approximately constant. As reported in Ref. [12], the slumping velocity is approximately constant at $\sqrt{2}/Fr$. In our simulations we found it to be 1.42/Fr. The current eventually slows beginning around time 12. We note that a
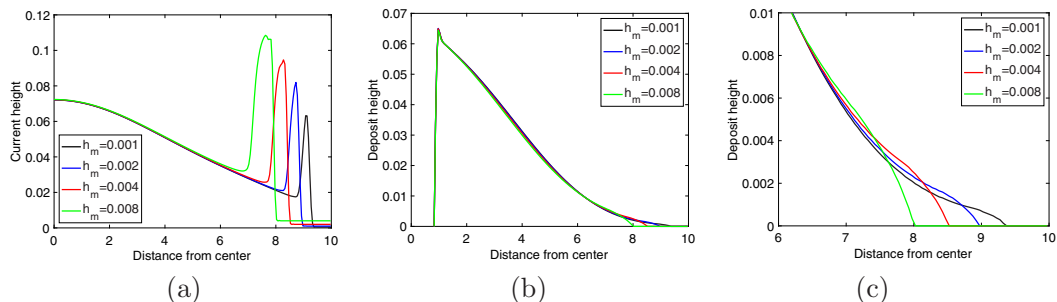
FIG. 7. (a) Current height and (b) resulting deposit height normalized by D/L for various values of the minimum height h_m. Other parameters are as shown in Table II and we show a cut from the center of the domain in a direction perpendicular to the vehicle motion. (c) Closeup of the deposit height at the front where variations are most pronounced.

similar slumping phase and velocity were obtained for axisymmetric currents in our simulations, which corresponds to a faster spread than predicted by the box model. As a result, we expect the accuracy of our simulations to be greater for currents spreading unidirectionally, so in the regime $\text{Fr}^2 > 2$. A comparison of our results to direct numerical simulations of the current generated by a moving source is presented in the next section.

From our validation, we conclude that the front dynamics may not be captured perfectly accurately with the parameters used to allow for faster computations. The effects on the current height of using a larger h_m and smaller Re_n than ideal are opposite of each other, therefore partially canceling. Only the speed of the spread is reduced by both a too large h_m and a too small Re_n. However, their effects on the current shape is small for h_m and negligible for Re_n. Moreover, the long-term behavior of the current, notably the deposit left behind and the extent reached are virtually unaffected by these choices. We therefore focus our attention on these features in the rest of this paper.

VII. PHYSICAL RESULTS

We characterize in this section the effects of the particle settling speed, u_s, and of the vehicle Froude number, Fr, on the currents' time evolution and on the height of the deposits they leave behind. In the shallow-water equation model, a third physical parameter is present, the drag coefficient, C_D, though it does not have an equivalent in the box model. We investigated the effects
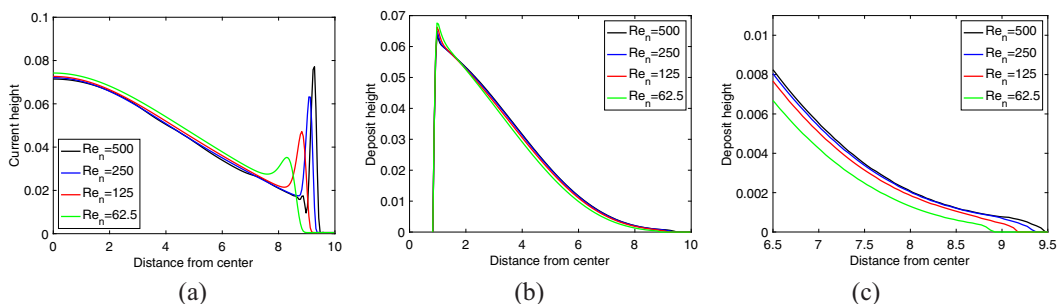

FIG. 8. (a) Current height and (b) resulting deposit height normalized by D/L for various values of the numerical Reynolds number (Re_n). Other parameters are as shown in Table II and we show a cut from the center of the domain in a direction perpendicular to the vehicle motion. (c) Closeup of the deposit height at the front where variations are most pronounced.
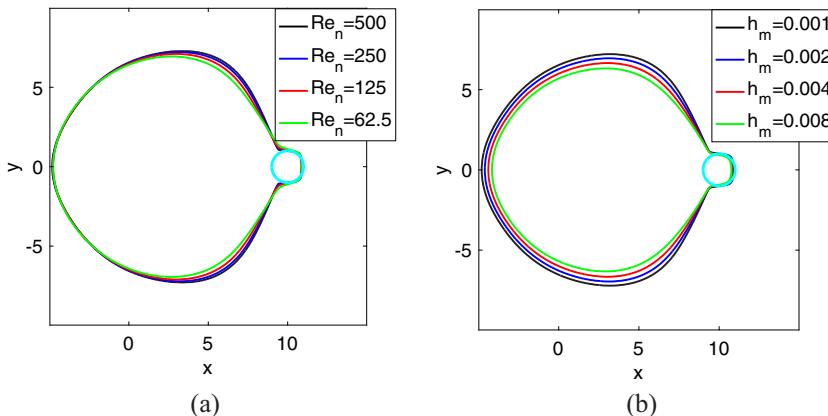
FIG. 9. (a) Contour of the current height $h = 2h_m$ for various numerical Reynolds numbers. (b) Contour of the current height $h = 2h_m$ for various minimum current heights h_m. Other parameters are as shown in Table II and the vehicle is shown as a cyan circle.

of the drag coefficient and found them to be mostly restricted to the vicinity of the vehicle, causing a broader front around the vehicle at larger C_D and resulting in a more pointed propagation front for $C_D = 0$. However, because these effects were localized and did not extend to the global features of the current, we focus here on the effects of u_s and Fr.

We note first that, as can be seen in Figs. 11 and 12, the SWE simulations yield a current that spreads significantly faster than the box model. In general, and even more so in axisymmetric currents [11], the SWE are known to over-predict the spread of gravity currents, and this is also the case here. Comparing our results to those of Ref. [8] (with our Fr^2 playing the role of their a^3), we note, for example, that our SWE simulations yield currents spreading faster than what is found in comparable direct-numerical simulations, while the BM results are in closer agreement, with, for example, the spreading rate of an axisymmetric current being only about 21% faster in our BM, despite the value of C_F being selected to agree with two-dimensional currents. Better agreement can
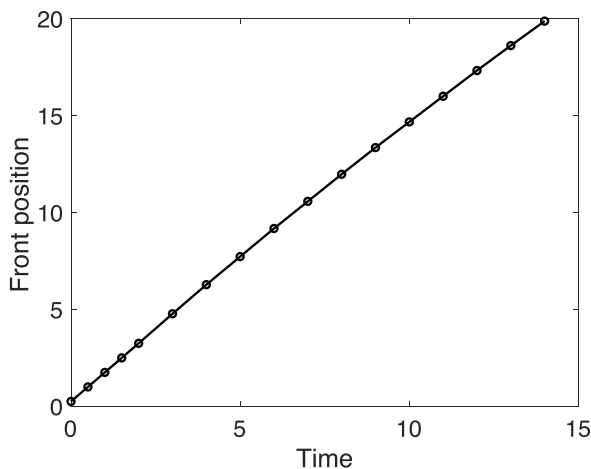

FIG. 10. Front position of a two-dimensional current with no source present as computed by the SWE. The slumping phase with constant velocity is recovered, with a computed velocity of 1.42.

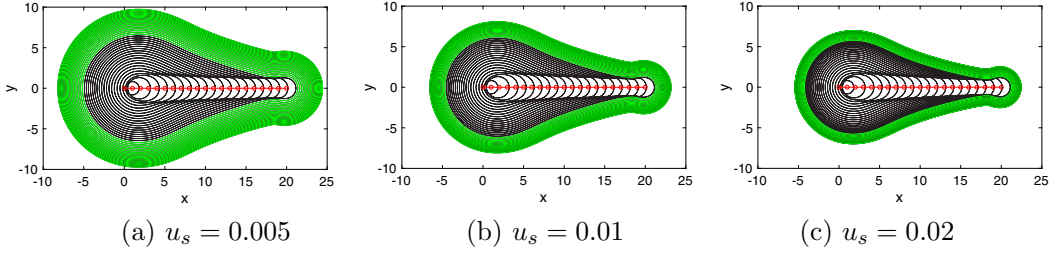(a) $u_s = 0.005$ (b) $u_s = 0.01$ (c) $u_s = 0.02$

FIG. 11. Box model simulated contours of the current boundary for (a) $u_s = 0.005$, (b) $u_s = 0.01$, and (c) $u_s = 0.02$. Here the vehicle position is shown with red circles and the black contours are the boundary until time $t = 20$, at which point the vehicle stops. Green contours are the boundary location after the vehicle has stopped moving. We set $\mathrm{Fr}^2 = 2$.

be achieved in the SWE by introducing additional parameters such as shape factors, entrainment coefficient, and drag terms [11], but these terms would not alter the qualitative trends found here in terms of u_s and Fr. To focus on the novel features of the moving source of a turbidity current, we do not introduce here these additional factors, but note that they could be added later if more data were available to determine their most appropriate values.
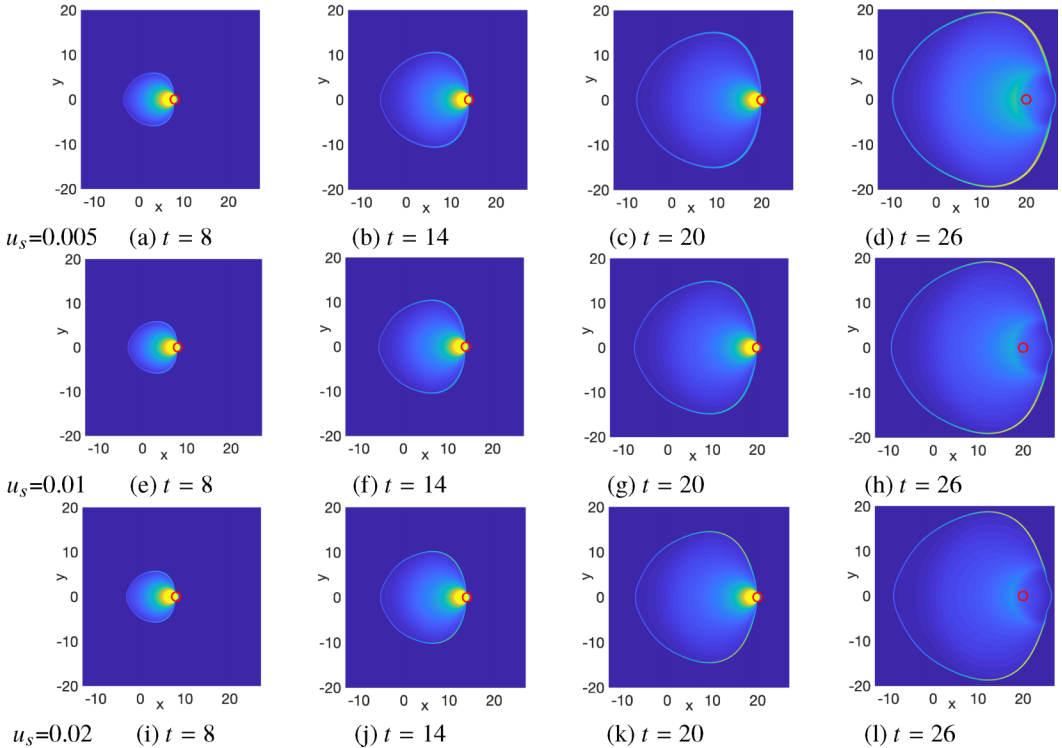
FIG. 12. Shallow-water equation simulated time evolution of the current height for [(a)–(d)] $u_s = 0.005$, [(e)–(h)] $u_s = 0.01$, and [(i)–(l)] $u_s = 0.02$. The vehicle is shown as a red circle and stops at time 20. Other parameters are $\mathrm{Fr}^2 = 2$ and $C_D = \pi/10$.
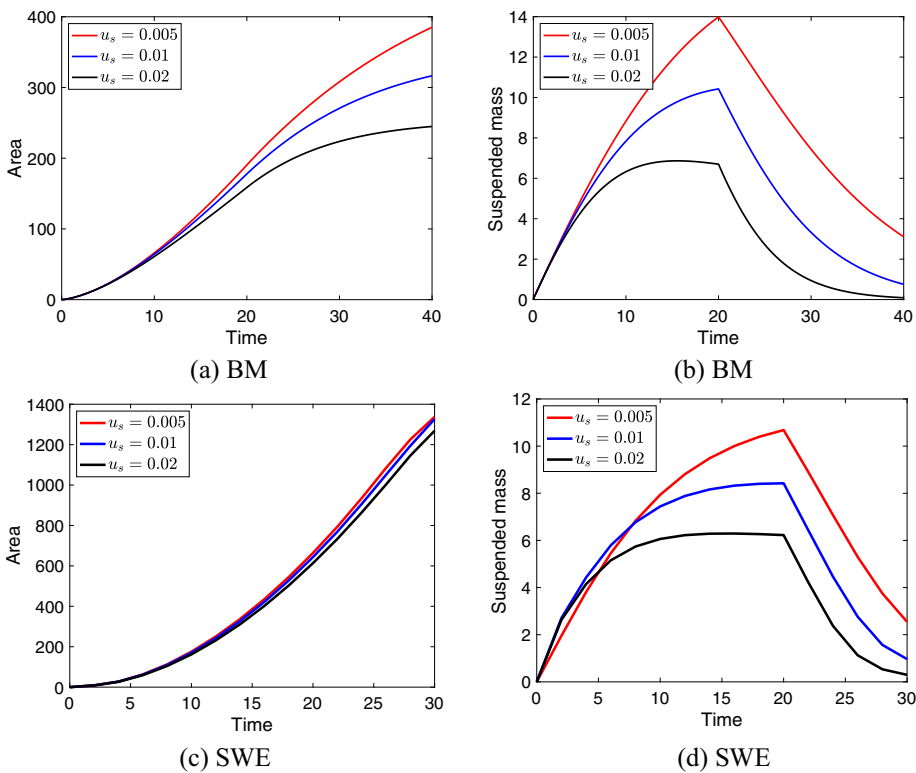
FIG. 13. Using the BM, (a) current area and (b) suspended mass as a function of time for various settling speeds. Using the SWE, (c) current area and (d) suspended mass as a function of time. Here the vehicle is moving until time $t = 20$, at which point it stops. Other parameters are $\mathrm{Fr}^2 = 2$ and, for SWE, $C_D = \pi/10$.

A. Effects of the settling speed

We used the BM to simulate gravity currents for various particle settling speeds, u_s, as shown in Fig. 11, and compare the results to those obtained from the SWEs, shown in Fig. 12. For the BM, we see that the current spreads in a similar way for all values of u_s while the vehicle is moving (prior to time $t = 20$, black contours), as the particle settling is dominated by the influx of new particles. However, the current spread is quickly affected by the particle settling speed as soon as the vehicle stops, with larger settling speeds corresponding to currents slowing down first. In the SWE simulations, the spread of the current seems to be even less affected by the value of u_s, at least for the time span considered. The propagation of the front, which includes inertial effects from the earlier stages of spread, is very similar for all the values of u_s presented. However, once the vehicle stops the current height closer to the vehicle path and away from the front is significantly higher for small particle settling speeds, as fewer particles have settled out.

Figure 13 presents a comparison of global features of the current as captured by the box model and by the shallow-water equations. While the vehicle is moving, the surface area of the current grows almost independently of the particle settling speed in both models. Even after the vehicle has stopped, the current area in the SWE model shows little dependence on u_s, most likely because the current head has a large height, as was seen in the validation section, rendering it less susceptible to particle settling. We also see that the SWE generate currents with much larger surface areas than the BM. However, the surface area in the SWE is defined here as the whole region within the contour $h = 2h_m$, as shown in Fig. 9, which includes regions where the current is very thin and therefore can be seen as an overestimation of the dynamically relevant area of the current. We also track
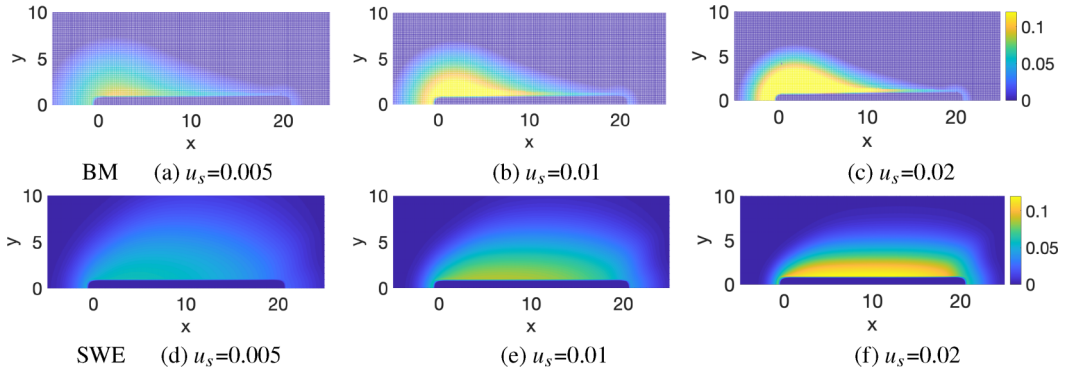
FIG. 14. [(a)–(c)] BM simulated deposit heights at time $t = 26$ for various particle settling speeds u_s. [(d)–(f)] Corresponding SWE simulated deposit heights at time $t = 26$. Other parameters are $\mathrm{Fr}^2 = 2$ and, for SWE, $C_D = \pi/10$.

the total mass of suspended particles, defined as $\Delta\rho_s c_b v_b$ for the box model and as the integral of $\Delta\rho_s \phi = \Delta\rho_s h\tilde{c}$ for the SWE. We find that it is quite similar in both models and shows a more clear dependence on the particle settling speed. While the vehicle is moving, the suspended mass initially grows quickly. For the largest settling speed considered here, $u_s = 0.02$, an equilibrium mass is then reached where settling balances newly resuspended particles. Presumably an equilibrium mass would eventually be reached for all particle settling speeds, but require more time to be established for smaller values of u_s. After the vehicle stops, the mass decreases in all cases, with a faster rate of decrease at higher u_s. Overall, the settling speed thus has a relatively weak influence on the current shape but a more significant effect on the amount of particles in suspension. This in turn will affect the shape of the deposit profiles left behind.

The height of the deposits found using the BM simulations have similar shapes for various u_s, with higher deposits in regions reached earlier by the current, see Figs. 14(a)–14(c), so that the boundary of the current over time approximates level curves of the deposit height. However, the height of the deposits near the vehicle path is sensitive to u_s, with larger settling speeds resulting in higher deposits, as seen in the color bars of Fig. 14, and correspondingly fewer particles left in suspension. The deposit heights obtained by the SWE, Figs. 14(d)–14(f), show similar trends and clearly show a broader deposit for smaller settling speeds. Comparing both methods, we note that the BM shows a much stronger dependence on the vehicle's starting point. The deposit heights obtained from the BM are increasing at the same rate for any point within the current, so that the longer a point has been covered by the current, the higher deposit it receives. At long times, this is likely to result in larger discrepancies between the two models, and the SWE results are more likely to be accurate, as regions that have been within the current for a long time become depleted of particles and no longer contribute to the deposit. This is clearly visible in Fig. 15, which shows a horizontal cut of the deposit height parallel to the vehicle's path. The SWE deposit heights are clearly more even, with larger deposits associated to larger u_s. The deposit height shape is peaked near the vehicle's starting point for the BM, particularly at higher particle settling speeds where the assumption of uniform concentration becomes more inaccurate. We show in Fig. 16 cuts of the deposit height taken perpendicular to the vehicle's path at three different locations. The results are rather similar between the two models for small x, but become more and more different as x increases and spatial nonuniformities grow.

B. Effects of the Froude number

We look next at the impact of the Froude number on the spreading current as simulated by the box model, Fig. 17, and by the shallow-water equations, Fig. 18. For $\mathrm{Fr}^2 = 0.5$, the current
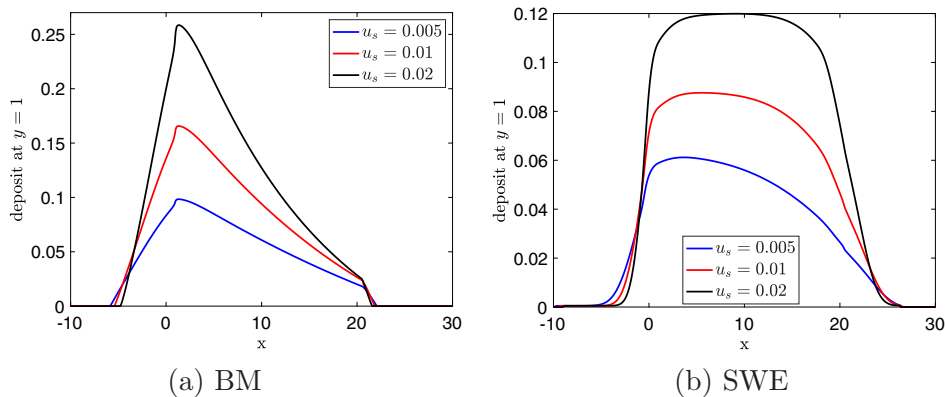
(a) BM (b) SWE

FIG. 15. Deposit height at time $t = 26$ at the level immediately to the side of the vehicle, $y = 1$ for various particle settling speeds u_s obtained (a) by the BM and (b) by the SWE. Other parameters are $\mathrm{Fr}^2 = 2$ and, for SWE, $C_D = \pi/10$.

spreads quickly perpendicular to the vehicle's motion, resulting in a more circular boundary. This is most evident at early times, when the particle concentration in the current is still relatively high. At longer times, the concentration is reduced and the current spreads more slowly, and eventually the vehicle motion becomes dominant in the BM simulations. This last feature is not observed in the SWE and is probably not realistic as the local concentration near the vehicle should be high even at later times. In SWE simulations, the front of the current spreads with approximate speed $\sqrt{2}$, so that we expect the overall dynamics to exhibit subcritical flow when $\mathrm{Fr}^2 < 2$ as the vehicle then moves slower than the current and therefore remains within the body of the current. This is observed in Fig. 18 for $\mathrm{Fr}^2 = 0.5$. The current then spreads so fast laterally that it reaches the

BM (a) $x = 2.5$ (b) $x = 10$ (c) $x = 17.5$

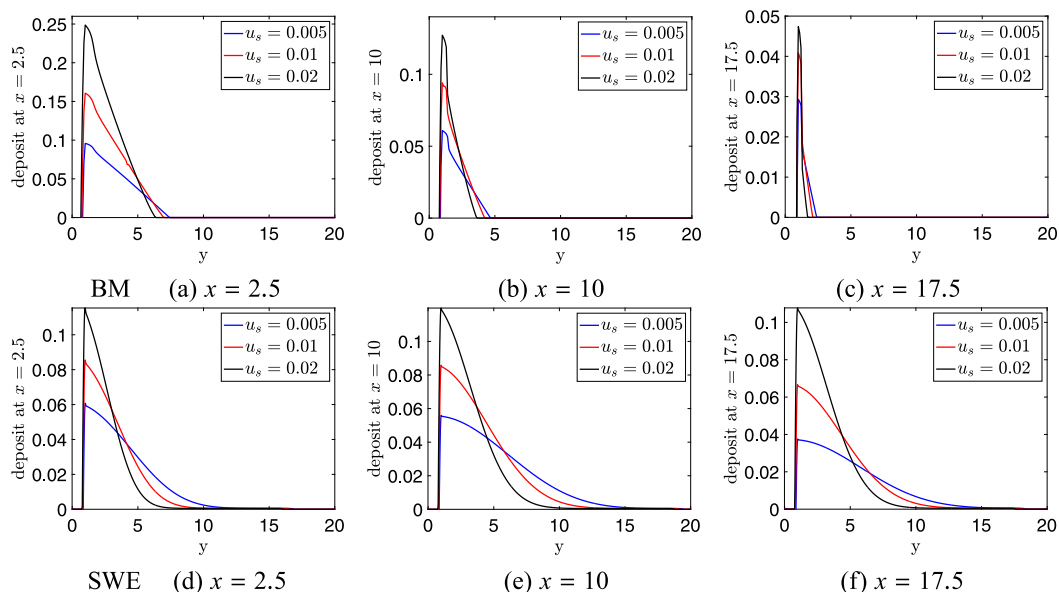SWE (d) $x = 2.5$ (e) $x = 10$ (f) $x = 17.5$

FIG. 16. Deposit heights at time $t = 26$ for various settling speeds, u_s, at the three points along the progression of the vehicle: $x = 2.5$, $x = 10$, and $x = 17.5$. Results are obtained [(a)–(c)] using the BM and [(d)–(f)] using the SWE. Other parameters are $\mathrm{Fr}^2 = 2$ and, for SWE, $C_D = \pi/10$.

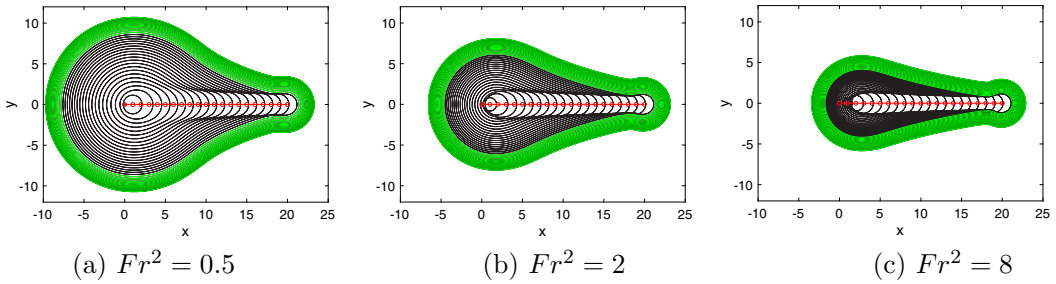(a) $Fr^2 = 0.5$ (b) $Fr^2 = 2$ (c) $Fr^2 = 8$

FIG. 17. Box model simulated contours of the current boundary for (a) $Fr^2 = 0.5$, (b) $Fr^2 = 2$, and (c) $Fr^2 = 8$. Here, the vehicle position is shown with red circles and the black contours are the boundary until time $t = 20$, at which point the vehicle stops. Green contours are the boundary location after the vehicle has stopped moving. We set $u_s = 0.01$.

spanwise boundaries of the computational domain used for the SWE, which has size 40 by 40 units, making the results at the last time shown $t = 26$ dependent on the boundary's location. At the other extreme, for $Fr^2 = 8$, the vehicle travels faster than the current, resulting in an elongated particle cloud, a feature qualitatively recovered by both models. The flow is then super-critical in that the current is then unable to catch-up to the vehicle. As shown in Ref. [8], the current spread is then mostly span-wise and develops as would a two-dimensional current launched by the moving vehicle,
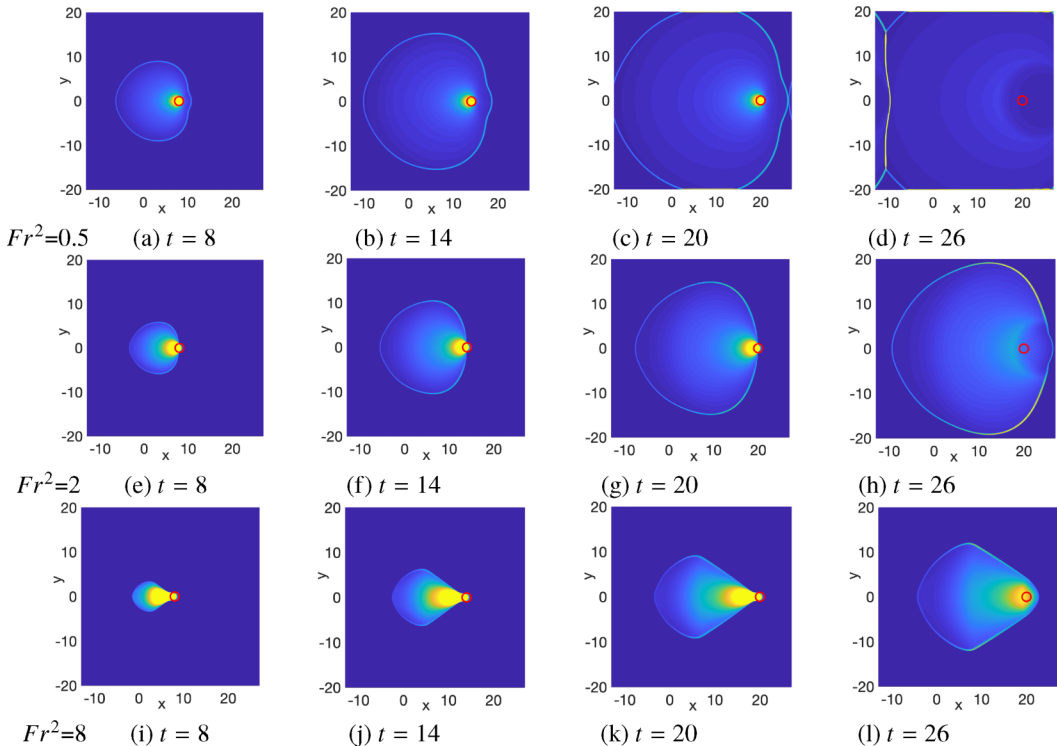

FIG. 18. Shallow-water equation simulated time evolution of the current height for [(a)–(d)] $Fr^2 = 0.5$, [(e)–(h)] $Fr^2 = 2$, and [(i)–(l)] $Fr^2 = 8$. The vehicle is shown as a red circle and stops at time 20. Other parameters are $u_s = 0.01$ and $C_D = \pi/10$.

(a) $Fr^2 = 2$　　　　(b) $Fr^2 = 4$　　　　(c) $Fr^2 = 8$　　　　(d) $Fr^2 = 16$
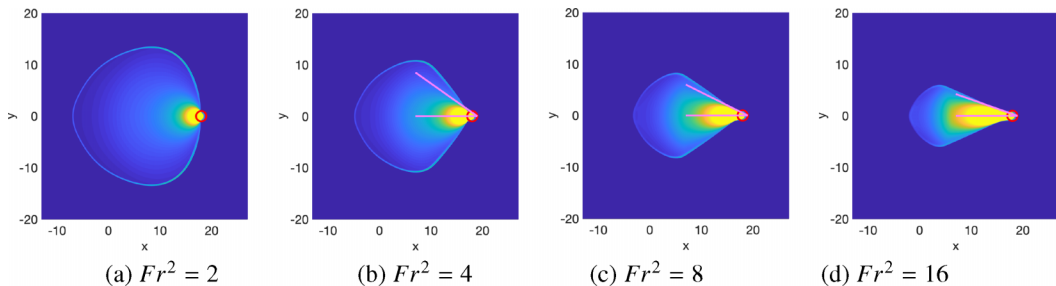
FIG. 19. Snapshots of the shape of a gravity current at time $t = 18$ for various Froude numbers as simulated by the shallow-water equations. The vehicle is shown as a red circle and the estimated opening angle with tangent $\sqrt{2}/\text{Fr}$ is shown in pink. Other parameters are $u_s = 0.01$ and $C_D = \pi/10$.

with no significant streamwise interactions until the vehicle stops. The intermediate case of $\text{Fr}^2 = 2$ shows a transition regime with a slight elongation, which is more pronounced in the box model than in the shallow-water equations, where the vehicle remains on the edge of the front of the current.

We show in Fig. 19 a snapshot of the current shape at a fixed time for various values of Fr^2. In the super-critical regime shown, the vehicle therefore precedes the spreading current and the slope of the opening front can be approximated as the ratio of the two-dimensional spreading velocity to the vehicle velocity, which here is approximately $\sqrt{2}/\text{Fr}$. This angle is shown in pink in Fig. 19 and can be seen to approximate the current front very well for $\text{Fr}^2 \geqslant 8$. Because currents in SWE simulations travel faster than what is reported in direct numerical simulations, the opening angle is greater than that reported by Ref. [8]. However, our simulations confirm the qualitative understanding that the current spreads away from the vehicle's path in a manner virtually identical to the spread of a two-dimensional turbidity current with a finite initial area. The consequences of this on the extent of the final deposit are discussed in the next section.

The global features of the suspended mass and current area as obtained by both models are shown in Fig. 20. Both models are seen to recover similar trends, with the only significant difference being the SWE simulations showing a much greater current area (about three times greater) in all cases. The currents with smaller Fr spread over a greater area, allowing more particles to settle out quickly, and resulting in a smaller suspended mass. For $\text{Fr}^2 = 0.5$, an equilibrium suspended mass is reached, and even overshot, while the vehicle is still moving. For the SWE simulations, the current area appears to level off at late times, but this is an artifact of the finite domain size used in the simulations.

We show the deposit heights left by the currents according to both models in Fig. 21. As was the case for the current shape, the deposits are more circular at low Fr and more elongated at high Fr. This effect is more accentuated in the BM. In fact, in the SWE, we see in Fig. 22 that the deposit height actually increases along the path of the vehicle at low Fr, as particles resuspended early settle ahead of the vehicle before additional particles are suspended and later settle as the vehicle arrives. Once again, the BM deposit heights increase uniformly over the entire current area, resulting in the highest deposit being located at the initial location of the vehicle. We see in Fig. 23 that the deposit heights along the y axis (away from the vehicle path) agree well between both models for small x, but become progressively more different as one moves in the direction of the vehicle motion (increasing x).

VIII. DISCUSSION AND CONCLUSION

Our simulations have allowed us to provide a clear description of the behavior of turbidity currents generated by a moving source, which we use to model the particle plume generated by an underwater vehicle. The derivation of the governing equations has shown that such currents
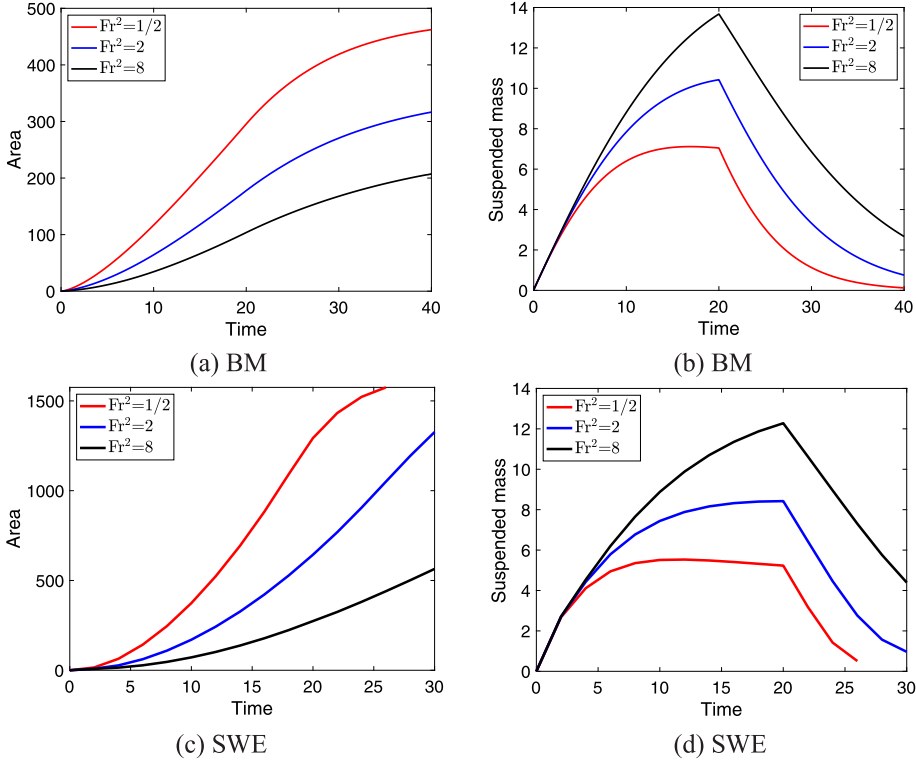
FIG. 20. Using the BM, (a) current area and (b) suspended mass as a function of time for various Froude numbers. Using the SWE, (c) current area and (d) suspended mass as a function of time. Here the vehicle is moving until time $t = 20$, at which point it stops. Other parameters are $u_s = 0.01$ and, for SWE, $C_D = \pi/10$.

are described by three nondimensional numbers: a drag coefficient C_D, a Froude number Fr $=$ $U_v/\sqrt{\Delta\rho_s C_p gD}$, and a dimensionless particle settling speed $u_s = U_s/U_v$. The flow near the vehicle itself is dependent on the choice of drag coefficient (C_D) or on how the flow past a vehicle is modeled in the box model. However, this is a localized effect and direct numerical simulations likely suffer
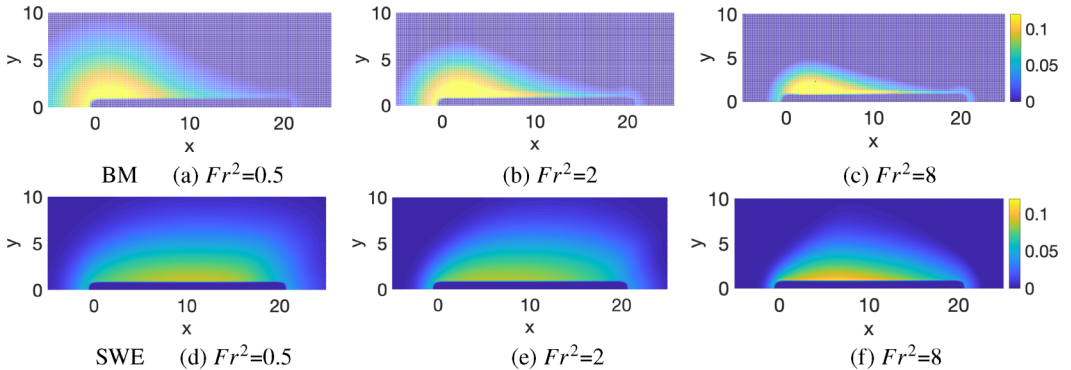

FIG. 21. [(a)–(c)] BM simulated deposit heights at time $t = 26$ for various Froude numbers Fr. [(d)–(f)] Corresponding SWE simulated deposit heights at time $t = 26$. Other parameters are $u_s = 0.01$ and, for SWE, $C_D = \pi/10$.
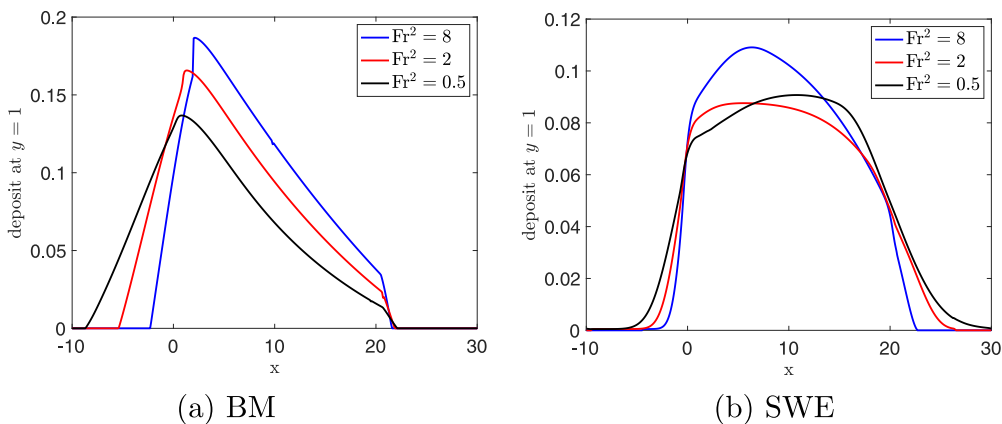
(a) BM

(b) SWE

FIG. 22. Deposit heights at time $t = 26$ at the level immediately to the side of the vehicle, $y = 1$, for various Froude numbers Fr obtained (a) by the BM and (b) by the SWE. Other parameters are $u_s = 0.01$ and, for SWE, $C_D = \pi/10$.

the same limitation unless they are able to resolve the exact shape of the vehicle. Overall, we found that the drag coefficient is relatively unimportant except for the immediate vicinity of the vehicle, and the other two dimensionless numbers are more influential.

Comparing the SWEs and BM results, we find that both approaches correctly capture the trends and dependencies on Fr and u_s but exhibit differences in other respects. The BM shows significant differences from the SWE when nonuniformities are present in the current. This is most visible at longer times and in the high Fr regime, where the source of particles gets to be far removed from
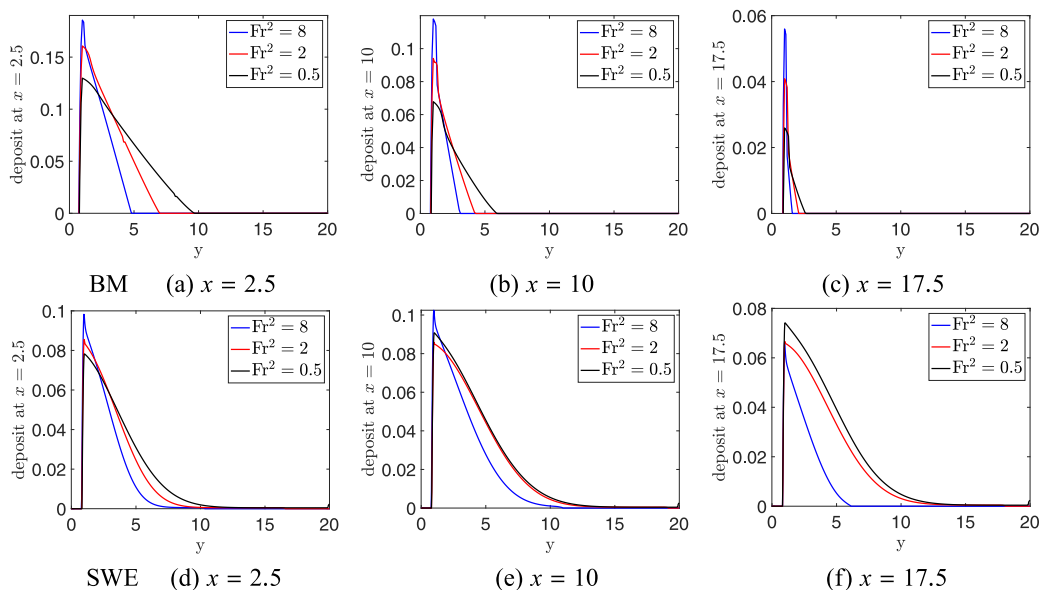

BM   (a) $x = 2.5$ (b) $x = 10$ (c) $x = 17.5$

SWE   (d) $x = 2.5$ (e) $x = 10$ (f) $x = 17.5$

FIG. 23. Deposit heights at time $t = 26$ for various Froude numbers, Fr, at the three points along the progression of the vehicle: $x = 2.5$, $x = 10$, and $x = 17.5$. Results are obtained [(a)–(c)] using the BM and [(d)–(f)] using the SWE. Other parameters are $u_s = 0.01$ and, for SWE, $C_D = \pi/10$.

some parts of the spreading current and the box model overestimates the spreading away from the vehicle. However, comparison with the simulations of Ref. [8] indicate that in the axisymmetric or near axisymmetric regime of Fr $\ll$ 1, the box model provides a good estimate of the current spreading rate. Moreover, for global quantities such as the suspended mass of sediments, the BM agrees well with the SWE and so can provide useful estimates.

Based on our validation, we find that the front head size in SWE simulations is sensitive to numerical parameters such as the minimum current height and the numerical Reynolds number. Moreover the SWE over-predict the spreading rate of the current, resulting in an overestimate of their area. This is a well-known issue for this formulation and previous authors (see Ref. [11] for a summary) have suggested several additional parameters that can be introduced to improve the agreement of the spreading rate computed by the SWE and experimental observations or direct numerical simulations. For example, a drag term of the form $-c_d|\bar{\boldsymbol{u}}|^2 = -c_d|\boldsymbol{q}/h|^2$ can be added in the momentum equation of the SWE [Eq. (12)], where c_d is a coefficient of magnitude approximately 0.05. Similarly, a shape factor, capturing the fact that the average over the current's height of $\boldsymbol{uu}$ is not, in general $\bar{\boldsymbol{u}}\bar{\boldsymbol{u}}$, can be introduced in the term $\nabla \cdot (\frac{\boldsymbol{qq}}{h})$. Perhaps more crucially, an entrainment coefficient capturing the mixing of ambient fluid into the current can also be added to the SWEs. This may be achieved by adding a term of the form $\eta|\bar{\boldsymbol{u}}|$ on the right-hand side of Eq. (11), and a similar treatment may be applied to the box model, with $\eta \approx 0.1$. These terms are usually most useful for, but not restricted to, currents spreading over a sloping bottom. Although incorporating these additional parameters could certainly improve quantitative agreement, they would most likely not affect any of the trends discussed here. Importantly, the spreading rate of the front had little effect on the core of the currents and on the height of their deposit and the SWE therefore provide descriptions of these features, which are dominant in the long-term fate of these currents, that are robust to changes in numerical parameters and compare well to previously published results in two-dimensional simulations, for example, in Ref. [16].

The Froude number, as the ratio of the vehicle speed to a typical current speed, controls the shape of the current. For Fr^2 > 2, the supercritical regime, the vehicle travels faster than the current spreads, resulting in more elongated currents with a pointed shaped near the vehicle. As recently shown by Ref. [8] and confirmed by our SWE simulations, the currents in this regime spread away from the vehicle in a manner similar to two-dimensional currents with a given initial area and no source term. Conversely, the subcritical regime, Fr^2 < 2, results in rounder currents, where the vehicle remains within its own particle cloud.

The effect of the particle settling speed on the current shape is relatively small, since the inertial components of the currents are dominant when $u_s \ll 1$. However, the breadth of the deposits, as well as their shape in the direction of the vehicle's motion are sensitive to u_s. Larger settling speeds result in deposits that are higher near the vehicle's path and have a smaller transversal extent. Smaller settling speeds generate broader deposits which also show a higher deposit near the starting point of the vehicle. At long times, an equilibrium mass of suspended particles can be reached (it was reached in some of our simulations but not all) where the resuspension of particles due to the vehicle balances the particles settling from the current. This equilibrium mass is smaller and is reached faster for large values of u_s and small values of Fr.

The insight obtained from both sets of simulations and from the results of Ref. [8] allows us to quantify the maximum extent of the deposits resulting from turbidity currents due to a moving source in both the subcritical and the super-critical regimes. First, in the super-critical regime Fr^2 > 2, where the vehicle always moves faster than the current spreads, the spanwise spread is effectively that of a two-dimensional turbidity current. In this case, it is known [16] that the maximum extent of the deposit can be approximated as

$$r_m \approx 2\left(\frac{C_0 A_0}{\text{Fr}^2 \, u_s^2}\right)^{1/5} \quad \text{if Fr}^2 > 2, \tag{23}$$
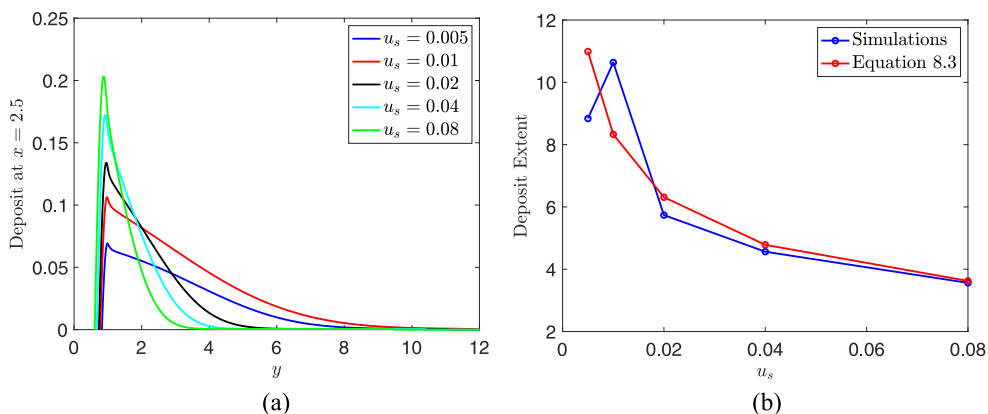
FIG. 24. (a) Spanwise deposit heights at time $t = 26$ for various settling speeds u_s at high Froude number, $\mathrm{Fr}^2 = 8$, at streamwise location $x = 2.5$. (b) Maximum extent of the deposits, defined, over all values of x, as the greatest value of y where the deposit exceeds 0.001, as a function of settling speed. Results are compared to Eq. (23), shown as the red line.

where A_0 is the initial area of the current and C_0 its initial concentration. For a moving vehicle, the initial area is one (dimensionally L^2) and the initial particle concentration is also one (dimensionally D/L). In dimensional form, we therefore have a maximum spread of approximately

$$R_m \approx 2 L \left(\frac{gDC_p\Delta\rho_s}{U_s^2} \right)^{1/5} \quad \text{if } \mathrm{Fr}^2 > 2. \tag{24}$$

We note that in this regime the width of the deposit is independent of the vehicle's speed, a rather counterintuitive result. Simulations of the SWE in this regime, shown in Fig. 24 agree well with the prediction of Eq. (23), though for smaller u_s the SWE again over-predicts the spread of the current. Here the spread was taken as the distance where the deposit reached a height above 0.001. The currents for the smallest two settling speed eventually interacted with the computational domain boundaries, slowing their advance, and for $u_s = 0.005$ a large fraction of particles remained in suspension, resulting in a shorter recorded spread than what would have been reached in a larger domain. However, for $u_s \geqslant 0.02$, this was not an issue.

If $\mathrm{Fr}^2 \leqslant 2$, the spread initially resembles that of a quasisteady axisymmetric current due to a fixed source, which is well described by a box model. To approximate the maximum deposit extent in this regime, we first consider the box model of a current spreading from a stationary source. Using a constant dimensionless source of one, the volume of the current is simply the time t. Its area is πr_b^2 and its height is then $t/\pi r_b^2$. We can therefore write the rate of change of the current's area and particle concentration, c_b, as

$$\frac{d(\pi r_b^2)}{dt} = \frac{2\pi r_b C_F}{\mathrm{Fr}} \sqrt{\frac{c_b t}{\pi r_b^2}} = \frac{2\sqrt{\pi} C_F}{\mathrm{Fr}} \sqrt{c_b t}, \quad \text{and} \quad \frac{dc_b}{dt} = \frac{1 - (1 + u_s \pi r_b^2)c_b}{t}.$$

An approximate solution to these equations valid at long times is

$$\pi r_b^2 = \left(\frac{4\pi C_F^2}{\mathrm{Fr}^2 u_s} \right)^{1/3} t, \quad c_b = \left(\frac{\mathrm{Fr}}{2\sqrt{\pi} C_F u_s} \right)^{2/3} \frac{1}{t}. \tag{25}$$

We thus find that the rate at which the radius of the current spreads is

$$\frac{dr_b}{dt} = \left(\frac{C_F}{4\pi} \right)^{1/3} \frac{1}{\mathrm{Fr}^{1/3} u_s^{1/6}} \frac{1}{t^{1/2}}.$$

To estimate the time beyond which the effects of the source become negligible, t_M, we equate the spreading rate to the vehicle speed, which is one. At times greater than t_M, the source will move away faster than the current spreads, and its effects will therefore be negligible. We find that the spreading rate equals the vehicle speed for a radius r_M of

$$r_M = \left(\frac{C_F}{\sqrt{2\pi}} \right)^{2/3} \frac{1}{(\mathrm{Fr}^2 u_s)^{1/3}} \approx 0.42 \frac{1}{(\mathrm{Fr}^2 u_s)^{1/3}}, \tag{26}$$

which occurs at a time $t_M = r_M/2$. The concentration of particles at that time, c_M, can be estimated from Eq. (25) and the current volume is then $V_M = t_M$ (because current volume is generated at a nondimensional rate of one). The average current height is therefore $h_M = \frac{V_M}{\pi r_M^2} = \frac{1}{2\pi r_M}$.

After t_M, the current will continue to spread as a two-dimensional current of fixed area, reaching a maximum extent given by Eq. (23) where the initial concentration is c_M and the initial area is $r_M h_M = \frac{1}{2\pi}$. We thus find an additional spreading of

$$r^+ \approx 2 \left(\frac{r_M h_M C_M}{\mathrm{Fr}^2 \, u_s^2} \right)^{1/5} \approx 1.6 \frac{1}{\mathrm{Fr}^{2/15} \, u_s^{7/15}}.$$

This additional spreading is therefore like to be dominated by the contribution of $u_s^{-7/15}$, since the Froude number is raised to such a small power.

The total spread is then approximated by $r_m = r_M + r^+$, which is, in dimensional form,

$$R_m \approx 0.42 \, L \left(\frac{gDC_p\Delta\rho_s}{U_v U_s} \right)^{1/3} + 1.6 \left(\frac{gDC_p\Delta\rho_s U_v^5}{U_s^7} \right)^{1/15} \quad \text{if } \mathrm{Fr}^2 \leqslant 2. \tag{27}$$

This estimate neglects the initial size of the current and so is only expected to be valid if $R_m \gg L$. Our SWE results, shown in Fig. 16, show a dependency on u_s that is consistent with this scaling. However, to directly verify this criterion in the $r_m \gg 1$ regime where it is expected to be applicable would require using values of Fr and u_s that are smaller than what is currently accessible with our SWE simulations.

To see how these estimates can apply to deep-sea mining, we compute sample values of the maximum deposit extent for silt particles, with settling speed $U_s = 0.1$ mm/s, and for sand particles, with settling speed $U_s = 30$ mm/s [21]. We assume a vehicle size of $L = 2$ m and a scouring depth of $D = 10$ cm and consider inorganic particles with $\Delta\rho_s = 1.5$. In this case Fr $\approx U_v$ if the vehicle speed is expressed in m/s. We show in Fig. 25(a) the maximum deposit extent as a function of the vehicle speed. The transition from low to high Froude number occurs at $U_v \approx 1.4$, and the solid lines indicate the relevant maximum deposit, while the dashed lines are their continuations in the regime where they are no longer applicable. We note that in the low Fr regime, a minimum spread can be achieved by selecting the vehicle speed that minimizes Eq. (27). For vehicle speeds that are too slow, the deposit spreads effectively as from a stationary source to distances that can theoretically be boundless. For vehicle speeds that are sufficiently large to correspond to the high Froude number regime, the maximum deposit extent R_m becomes independent of U_v. We show in Fig. 25(b) how R_m depends on the particle settling speed in the high Fr regime, finding deposit extents of the order of tens of meters for sand particles and hundreds of meters for silt particles.

Future research should be aimed at quantifying the maximum spread of the deposits more accurately, especially in the intermediate regime where $\mathrm{Fr}^2 \approx 2$ and for small settling speeds that require larger computational domains. Our current implementation of the SWE is satisfactory, but it can be accelerated by considering a nonuniform or adaptive grid. This would allow to focus computational resources where they are most needed, i.e., in the vicinity of the vehicle and of the current's front, and overall would result in less computationally expensive simulations. Our models, both SWE and BM, may be used in the future to study more complex and realistic setups. Notably, one could incorporate the presence of a background current that may cause a drift of the particle cloud. The estimates of the deposit extent given here all assume a quiescent ambient fluid, but the
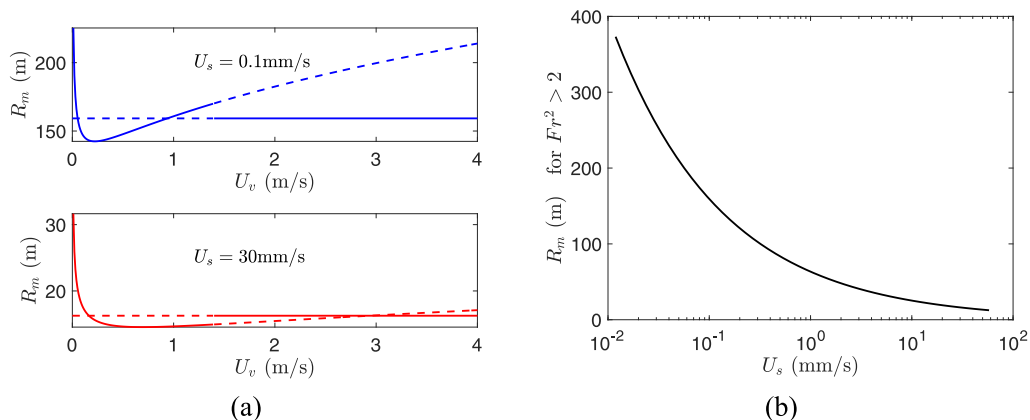
FIG. 25. (a) Maximum deposit extent, R_m, in meters for two different settling speeds corresponding to silt (top) and sand (bottom). The solid lines are the relevant maximum deposit curves based on the Froude number and the dashed lines are their continuations. Computations are made at high Froude number for $U_v > 1.4$ m/s using Eq. (24), and at low Froude number for $U_v < 1.4$ m/s using Eq. (27). Other parameters are $\Delta\rho_s = 1.5$, $L = 2$ m and $D = 10$ cm, so that Fr $\approx U_v$ if U_v is in m/s. (b) Maximum deposit extent in meters in the high Froude number regime, where R_m is independent of the vehicle speed, as a function of particle settling speed. Other parameters are as in panel (a).

presence of currents and regions of upwelling could significantly increase the size of the region over which particles may be redeposited, particularly silt and bacteria. The maximum extent described here thus provide a lower bound on the size of the region where particulates may be relocated. In addition, polydisperse systems can be simulated using the same approaches in a straightforward manner by considering several types of particles, each with their own concentration and settling speed. Such simulations can help determine if the presence of several particle sizes results in a behavior that is simply an average of what each type of particle would cause individually or whether the results are more complex. We may also study and even optimize more complex vehicular travel patterns to minimize the spread of suspended particles. This last problem requires very long time simulations and so is probably better tackled with the box model, provided the path chosen is relatively compact, such as a spiral. Studying final deposits as a function of path and vehicle speed is particularly helpful in selecting the least destructive manner to exploit deep-sea mining resources.

[1] J. R. Hein and A. Koschinsky, *Deep-Ocean Ferromanganese Crusts and Nodules in: Treatise on Geochemistry*, 2nd ed. (Elsevier, Amsterdam, 2013).

[2] T. Peacock and M. H. Alford, Is deep-sea mining worth it? Sci. Am. **318**, 72 (2018).

[3] M. V. Lindh, B. M. Maillot, C. N. Shulse, A. J. Gooday, D. J. Amon, C. R. Smith, and M. J. Church, From the surface to the deep-sea: Bacterial distributions across polymetallic nodule fields in the Clarion-Clipperton zone of the Pacific ocean, Front. Microbiol. **8**, 1696 (2017).

[4] H. J. Niner, J. A. Ardron, E. G. Escobar, M. Gianni, A. Jaeckel, D. O. B. Jones, L. A. Levin, C. R. Smith, T. Thiele, P. J. Turner, C. L. Van Dover, L. Watling, and K. M. Gjerde, Deep-sea mining with no net loss of biodiversity: An impossible aim, Front. Mar. Sci. **5**, 1 (2018).

[5] D. Aleynik, M. E. Inall, A. Dale, and A. Vink, Impact of remotely generated eddies on plume dispersion at abyssal mining sites in the Pacific, Sci. Rep. **7**, 16959 (2017).

[6] B. Gillard, K. Purkiani, D. Chatzievangelou, A. Vink, M. H. Iversen, and L. Thomsen, Physical and hydrodynamic properties of deep sea mining-generated, abyssal sediment plumes in the Clarion Clipperton Fracture Zone (eastern-central Pacific), Elem. Sci. Anth. **7**, 5 (2019).

[7] P. P. E. Weaver, J. Aguzzi, R. E. Boschen-Rose, A. Colaço, H. de Stigter, S. Gollner, M. Haeckel, C. Hauton, R. Helmons, D. O. B. Jones, H. Lily, N. C. Mestre, C. Mohn, and L. Thomsen, Assessing plume impacts caused by polymetallic nodule mining vehicles, Marine Policy **139**, 105011 (2022).

[8] R. Ouillon, E. Meiburg, and T. Peacock, Gravity currents from moving sources, J. Fluid Mech. **924**, A43 (2021).

[9] M. J. Castro and M. Semplice, Third- and fourth-order well-balanced schemes for the shallow-water equations based on the CWENO reconstruction, Int. J. Numer. Meth. Fluids **89**, 304 (2019).

[10] E. F. Toro, *Shock-capturing Methods for Free-surface Shallow Flows* (Wiley, New York, NY, 2001).

[11] M. Ungarish, *An Introduction to Gravity Currents and Intrusions* (CRC Press, Boca Raton, FL, 2009).

[12] H. A. Shimizu, T. Koyaguchi, and Y. J. Suzuki, A numerical shallow-water model for gravity currents for a wide range of density differences, Progr. Earth Planetary Sci. **4**, 8 (2017).

[13] T. Tran-Duc, N. Phan-Thien, and B. C. Khoo, A smoothed particle hydrodynamics (SPH) study on polydisperse sediment from technical activities on seabed, Phys. Fluids **30**, 023302 (2018).

[14] T. Tran-Duc, N. Phan-Thien, and B. C. Khoo, A three-dimensional smoothed particle hydrodynamics dispersion simulation of polydispersed sediment on the seafloor using a message passing interface algorithm, Phys. Fluids **31**, 043301 (2019).

[15] W. B. Dade and H. E. Huppert, A box model for nonentraining suspension-driven gravity surges on horizontal surfaces, Sedimentology **42**, 453 (1995).

[16] A. J. Hogg, M. Ungarish, and H. E. Huppert, Particle-driven gravity currents: asymptotic and box model solutions, Eur. J. Mech. B Fluids **19**, 139 (2000).

[17] C. Gladstone and A. W. Woods, On the application of box models to particle-driven gravity currents, J. Fluid Mech. **416**, 187 (2000).

[18] T. C. Harris, A. J. Hogg, and H. E. Huppert, A mathematical framework for the analysis of particle-driven gravity currents, Proc. R. Soc. London A **457**, 1241 (2001).

[19] E. Meiburg and B. Kneller, Turbidity currents and their deposits, Annu. Rev. Fluid Mech. **42**, 135 (2010).

[20] F. Necker, C. Härtel, L. Kleiser, and E. Meiburg, Mixing and dissipation in particle-driven gravity currents, J. Fluid Mech. **545**, 339 (2005).

[21] A. B. Valsangkar and N. V. Ambre, Distribution of grain size and clay minerals in sediments from the index area, central indian basin, Mar. Georesour. Geotechnol. **18**, 189 (2000).

[22] E. A. Spiegel and G. Veronis, On the boussinesq approximation for a compressible fluid, Astrophys. J. **131**, 442 (1960).

[23] H. Chowdhury, H. Moria, I. K. A. Ali, F. Alam, and S. Watkins, A study on aerodynamic drag of a semi-trailer truck, Procedia Eng. **56**, 201 (2013).

[24] P. Augier, A. V. Mohanan, and E. Lindborg, Shallow water wave turbulence, J. Fluid Mech. **874**, 1169 (2019).

[25] H. E. Huppert and J. E. Simpson, The slumping of gravity currents, J. Fluid Mech. **99**, 785 (1980).

[26] T. Benjamin, Gravity currents and related phenomena, J. Fluid Mech. **31**, 209 (1968).

[27] C. Shu, WENO methods, Scholarpedia **6**, 9709 (2011).

[28] M. de la Asunción, M. J. Castro, E. D. Fernández-Nieto, J. M. Mantas, S. O. Acosta, and J. M. González-Vida, Efficient GPU implementation of a two waves TVD-WAF method for the two-dimensional one layer shallow water system on structured meshes, Comput. Fluids **80**, 441 (2013).

[29] C. S. Peskin, The immersed boundary method, Acta Numerica **11**, 479 (2002).

[30] J. E. Simpson, *Gravity Currents in the Environment and the Laboratory*, 2nd ed. (Cambridge University Press, Cambridge, UK, 1997).